Magnetic and Structural Investigation of Manganese Doped SnO_2 and In_2O_3 Nanocrystals

by

Tahereh Sabergharesou

A thesis
presented to the University of Waterloo
in fulfillment of the
thesis requirement for the degree of
Master of Science
in
Chemistry - Nanotechnology

Waterloo, Ontario, Canada, 2013

AUTHOR'S DECLARATION

I hereby declare that I am the sole author of this thesis. This is a true copy of the thesis, including any required final revisions, as accepted by my examiners.

I understand that my thesis may be made electronically available to the public.

Abstract

Diluted magnetic semiconductor oxides (DMSOs) have received great attention recently due to their outstanding applications in optoelectronic and spintronic devices. Ever since the initial observation of ferromagnetism at room temperature in cobalt-doped titania, extensive effort is concentrated on preparation of transition metal doped wide band gap semiconductors, especially Mn-doped ZnO. Compared to Mn-doped ZnO, magnetic interactions in SnO_2 and In_2O_3 semiconductors have been underexplored. SnO_2 and In_2O_3 semiconductors have many applications, owing to their high charge carrier density and mobility as well as high optical transparency.

Investigation on electronic structure changes induced by dopants during the synthesis procedure can effectively influence magnetic interactions between charge carriers. In this work, a combination of structural and spectroscopic methods was used to probe as-synthesized SnO_2 and In_2O_3 nanocrystals doped with Mn^{2+} and Mn^{3+} as precursors. X-ray absorption near edge structure (XANES) and extended X-ray absorption fine structure (EXAFS) spectroscopy are powerful techniques to explore formal oxidation state of manganese dopant, electronic environment, number of nearest neighbors around the absorbent, and bond lengths to the neighboring atoms. Analysis reveals the presence of multiple oxidation states in the doped nanocrystals, and establishes a relation between $\frac{Mn^{2+}}{Mn^{3+}}$ ratio and expansion or contraction of lattice parameters.

Although doping semiconductors are crucial for manipulating the functional properties, the influence of dopants on nanocrystals structure is not well understood. Nanocrystalline films prepared from colloidal Mn-doped SnO_2 and In_2O_3 nanocrystals through spin coating process exhibit ferromagnetic behavior in temperatures ranging from 5 K to 300 K. Magnetic transformation from paramagnetic in free-standing Mn-doped nanocrystals to strong ferromagnetic ordering in nanocrystalline films is attributed to the formation of extended structural defects, e.g., oxygen vacancies at the nanocrystals interface. Magnetic circular dichroism (MCD) studies clearly show that Mn^{3+} occupies different symmetry sites in indium oxide, when bixbyite and rhombohedral In_2O_3 nanocrystals (NCs) are compared.

Acknowledgements

Praise and thanks to Allah, the Almighty, for His mercy endures forever and for His blessings.

This dissertation would not have been possible without the assistance of so many people: I would like to express my deepest appreciation and gratitude to my supervisor Dr. Pavle V. Radovanovic for all his precious support throughout this project. I would like to thanks his constructive comments, patience and his passion in science that have encouraged me to face many difficulties during my M.Sc. program.

I am also grateful to the members of my advisory committee, Dr. Jonathan Baugh and Dr. Holger Klienke for their constructive comments and insightful feedback on the thesis.

I am indebted to many people who have supported me in my academic career with their helpful comments and advices. I would like to give a very special acknowledgement to Dr. Eric Prouzet, who was always eager to help and giving his best suggestions and comments during the past years. I wish to express my gratitude to Dr. Ian D. Hosein who has inspired me and spared a lot of time out of his busy duties to give me great advices.

I could not have completed this research without the support of faculty, administrative staffs, friends and fellow graduate students in Chemistry department. I can't thank my colleagues and my friends enough, I had the pleasure to work with and learn a lot from them. I extent my sincere thanks to all of my group members especially Shokouh Farvid, Ling Ju, and Ting Wang.

The last but not least, I express my heartfelt gratitude to my parents and my siblings for their supports and abiding love. They have been always there for me, encouraged me, and gave me energy to achieve my goals despite the long distance between us. A special word of thanks to my husband, Masoud Ansari. During the most challenging years of my life his loving kindness helped me to keep standing and cope with my ongoing struggle. His support during these years was more invaluable to me than he knows, and I will continue to appreciate it for the rest of my life.

Table of Contents

List of Figures

List of Tables

.

List of abbreviations

bcc	Body-centered cubic
CN	Coordination number
DMS	Diluted magnetic semiconductor
DMSO	Diluted magnetic semiconductor oxide
EXAFS	Extended X-ray absorption fine structure
FFT	Fast Fourier transform
FWHM	Full width at half maximum
HRTEM	High-resolution transmission electron microscopy
LCP	Left circularly polarized
MCD	Magnetic circular dichroism
NC	Nanocrystal
PPMS	Physical property measurement system
RCP	Right circularly polarized
rh	Rhombohedral
RT	Room temperature
TCO	Transparent conducting oxide
TEM	Transmission Electron Microscopy
TM	Transition metal
TOPO	Tri-n-octylphosphine oxide
UV	Ultraviolet
Vis	Visible
XANES	X-ray absorption near edge structure
XAS	X-ray absorption spectroscopy
XRD	X-ray diffraction

Chapter 1
Introduction

1.1 Diluted Magnetic Semiconductor Oxides

Introducing ferromagnetic properties through spin functionality of a dopant into a non-magnetic semiconductor crystal has received a great attention over the last decade. In this group of materials, that have been categorized as diluted magnetic semiconductors (DMS), one can take the advantage of both parental properties: charge of electrons in semiconductors and electron spin of magnetic dopant element. Thus, information carried by the spin of electrons can add more degrees of freedom in novel electronic devices. Such a combination of properties makes them suitable for fabrication of integrated spintronic devices.[1, 2]

As shown by Dietl *et al,*[3] wide band gap semiconductors are one of the most promising materials for achieving high Curie temperatures. Their prediction shows ferromagnetism at room temperature in

Table 1-1: Material properties for semiconducting oxides.[4]

Compound	Crystal structure	Conductivity (s^{-1})	Carrier type	Maximum mobility ($cm^2V^{-1}s^{-1}$)	Band gap (eV)	Maximum Carrier concentration (cm^{-3})
$CuAlO_2$	Hexagonal	1	p	10	3.5	1.3×10^{17}
$CuGaO_2$	Hexagonal	0.063	p	0.25	3.6	1.7×10^{18}
$SrCu_2O_2$		0.05	p	0.5	3.3	6×10^{17}
$AgInO_2$	Hexagonal	6	n	0.5	4.2	2.7×10^{19}
ZnO	Hexagonal	20	n	200	3.2	1×10^{21}
In_2O_3	Cubic	10^4	n	30	3.75	1×10^{18}
Cd_2SnO_4	Orthogonal	10^4	n	40	2.7	
SnO_2	Tetragonal	10^4	n	10	3.6	8×10^{20}
TiO_2	Tetragonal		n	20-100	3.0	1×10^{19}
Cu_2O	Cubic		p	100	2.0	1×10^{17}

p-type GaN, or ZnO doped with 5% Mn.[3] In addition to ZnO, other semiconducting oxides have been considered.

Table 1-1 presents material properties of a number of diluted magnetic semiconductor oxides in which charge carriers are supposed to mediate ferromagnetic interactions.

1.1.1 Tin Oxide Crystal Structure

A good example of DMSO materials is tin oxide (SnO_2). Tin(IV) oxide (SnO_2) is a wide band gap (3.6 eV) transparent conductive oxide.[5] Tin oxide thin films with thickness of 0.1-1 μm show 97% optical transparency in the visible region, which makes it a good candidate for transparent conducting oxide applications. Metal catalytic centers in tin oxide nanoparticles result in boost of sensitivity as a gas detector. Good activity of tin oxide based catalyst towards CO/O_2 and CO/NO reactions makes it suitable as a heterogeneous catalyst.[6, 7]

As a mineral, SnO_2 is also called cassiterite. The crystal structure, rutile, is similar to many other metal oxides like TiO_2, RuO_2, MnO_2, CrO_2 and VO_2.[8] According to the Wyckoff rules, the rutile structure has a tetragonal unit cell with space group symmetry $P4_2/mnm$ (D_{4h}). The lattice constants are a= b= 4.74 Å and c= 3.18 Å with c/a ratio of 0.67. The unit cell contains six atoms, which are two tin atoms and four oxygen atoms. In the SnO_2 matrix, a quasi-regular octahedron is composed of oxygen atoms surrounding the tin atom that is sitting at the center. In the case of oxygen, three tin atoms surround oxygen and form approximately an equilateral triangle. The position of cations in the unit cell is (0,0,0) and $(\frac{1}{2}, \frac{1}{2}, \frac{1}{2})$ and anions are located at ±(u,u,0) and ±(u+$\frac{1}{2}$, u-$\frac{1}{2}$, $\frac{1}{2}$) where u= 0.307. A representative of the unit cell can be found in Figure 1-1. In addition to the rutile SnO2, Suito[9] et al. has found a dense form of orthorhombic SnO_2 at 15.8 GPa and 800 °C, and the boundary separating these two phases has been represented by P(kbar)= 140.0+ 0.022 T (°C).

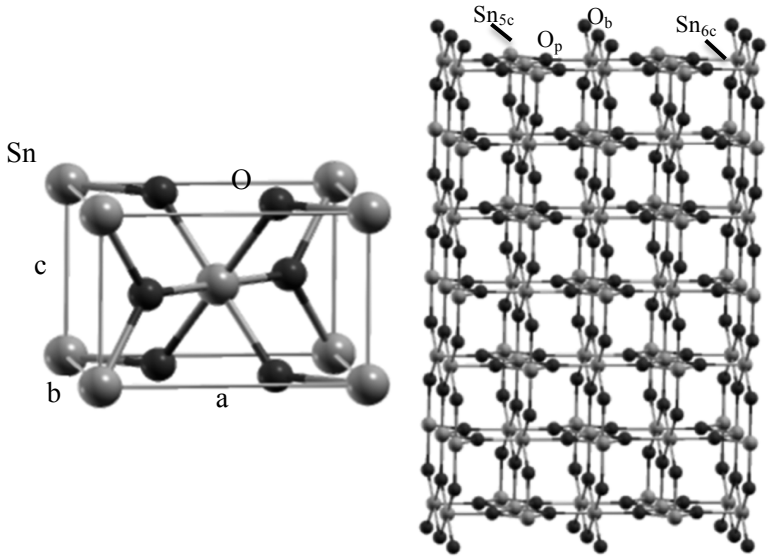

Figure 1-1: Rutile tetragonal unit cell of SnO_2.[10]

1.1.2 Indium oxide crystal structure

Indium oxide (In_2O_3) is a wide band gap, n-type semiconductor with an energy gap at room temperature of 3.55-3.75 eV.[11-13] The concurrent occurrence of high optical transparency and wide band gap make indium oxide a suitable candidate for electro-optic modulators, low-emissivity windows, solar cells, flat-panel displays, electrochromic mirrors, and sensors.[13-15]

Indium oxide crystalizes in two phases: the cubic type and metastable rhombohedral type. The cubic structure is also referred as bixbyite Mn_2O_3 or C-type rare earth oxide structures (rare earth is a crystal prototype structure, not the elements). According to the Wyckoff[8] the bcc-In_2O_3 unit cell with space group Ia3 consists of 16 molecules with 80 atoms with the lattice constant a=10.118 Å. In this lattice, 8 of the 32 cations sit on site b and the other 24 are in d-site. The bixbyite structure is made of edge-sharing InO_6 octahedra arranged in a 2×2×2 array. The b-site, like d-site, is six-fold coordinated by oxygens in a distorted octahedral geometry with In-O bond distance of 2.18 Å. In the b-site, two interstitial sites are located at body-diagonal positions of the cubic structure. In d-site structure, vacancies occupy the facial-diagonal sites with each two oxygen atoms in distances of 2.13, 2.19 and 2.23 Å.[16] Figure 1-2 (b) reveals the difference in the symmetry between 24d sites and 8b sites. B-site is centrosymmetic (S_6 or C_{3i} symmetry), while d-site shows a noncentrosymmetric (C_2) state.[17] Differences in the symmetry of b- and d-site, cations show distinct spectroscopic properties in these two sites.

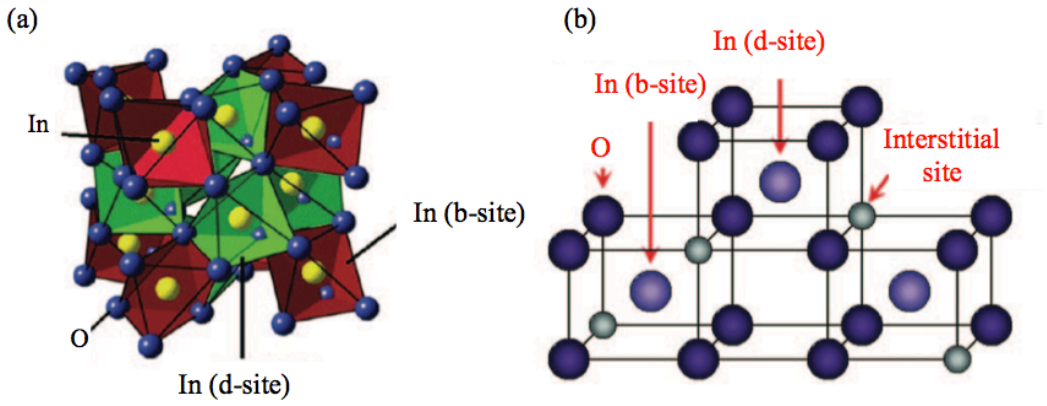

Figure 1-2: (a) In_2O_3 bixbyite structure containing octahedra (yellow: indium atom and blue: oxygen atom) (b) different vacancies positions in b-site and d-site.[17]

Shannon[18] has described one of the first reports on the formation of metastable rhombohedral (corundum) indium oxide (rh-In_2O_3). Phase transformation from bixbyite to rhombohedral can happen at elevated temperature and pressure (6.5 GPa and 125 °C); elimination of the pressure will not change the crystal structure. Stability of rh-In_2O_3 has been observed up to 12 GPa and 900 °C. Although initial study claims that rh-In_2O_3 is a high-pressure product, but recent reports present the formation of rh-In_2O_3 under ambient conditions (1bar, 250 °C).[19] Rhombohedral structure with space group $R\bar{3}c$ can be considered as an arrangement of hexagonal close pack oxygens, which is slightly distorted, and In^{3+} cations lying in two-thirds of the octahedral holes in the oxygen sublattice. The lattice parameters are $a = 5.49$ Å and $c = 14.52$ Å (Figure 1-2). In this arrangement, the six coordinated In^{3+} cations are surrounded with three oxygens in distance of 2.07 Å and three in 2.27 Å. [19] The unit cell with six formula units contains 12 In and 18 O (Figure 1-3).

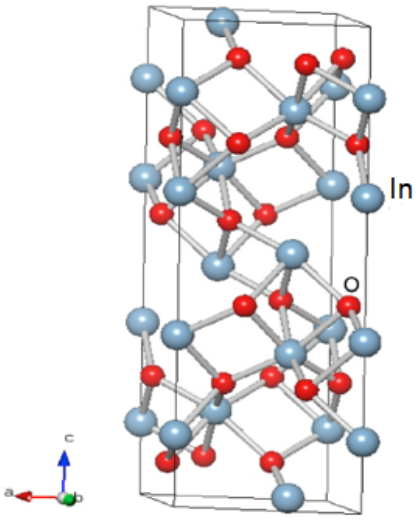

Figure 1-3: One unit cell of In_2O_3: the large and small spheres represent the In and O atoms, respectively.[20]

1.2 Doping DMSO Nanoparticles

SnO_2 and In_2O_3 as examples of transparent conductive oxides (TCOs), are widely used in optoelectronic devices,[21] flat panel displays,[22] solar cells,[23] and spintronics.[24] The focus of studies in the area of spintronics has largely been on the modification of the compositions and properties of nanocrystals by intentional incorporation of impurities, to form the class of materials known as diluted magnetic semiconductor oxides (DMSOs).

As an example of enhancing conductivity of semiconductors, one can consider extrinsic semiconductors. The impurities substitute elements of the host lattice adding either free electrons or forming holes in the crystal structure. So, there are two types of the semiconductors: the n-type (negative) in which the impurity has one more electron than the host atom and current carriers (electrons) are negative, and the p-type (positive), in which the impurity with one less valence electron substitutes for the host atom and positively charged holes move and carry the current.

1.2.1 Structural Characterization of DMSO Nanocrystals

The exact location of the dopant in the host lattice is the primary information needed to understand the precise role of dopant in modifying the properties of diluted magnetic semiconductor oxides

(DMSOs). This is a problem that cannot be resolved by applying conventional diffraction techniques. The problem may be more complicated when the dopant concentration is very low (less than 1 %mol), as the dopant is indistinguishable from the host atom (e.g., atoms with close atomic numbers are not discerned in conventional X-ray diffraction method), the dopant may introduce complex disorder into the host lattice, or the material is not crystalline. There is also a possibility of forming secondary phases too small to be observed. Therefore, it is crucial to employ other techniques to obtain vital structural information, and X-ray Absorption Spectroscopy (XAS) is particularly suited to solve this problem.

XAS spectroscopy is very powerful in probing the local structure to about 4 Å from the X-ray absorbing atom.[25] Extended X-ray Absorption Fine Structure (EXAFS) spectroscopy can be used for direct determination of the local structure in terms of the average number and distance of nearest neighbors of the cation site absorbing the X-rays. Also, the X-ray absorption data at the vicinity of the absorption edge, called X-ray Absorption Near Edge Structure (XANES), discloses information about oxidation state of the cation and provides a qualitative indication of site symmetry.

Rockenberger *et al.*[26] have investigated the effect of annealing on electrical conductivity for 2-6 nm Sb-doped SnO_2. Sb K-edge EXAFS measurement at 5 K proves incorporation of the antimony into tin dioxide lattice of a sample dried at 100 °C and 500 °C, respectively. Sb L_1-edge XANES reveals that although Sb^{III} has been used as a precursor, the doped samples have a high concentration of Sb^{V} before annealing at 500 °C in air (Figure 1-4). High temperature annealing of 9.1% and 16.7% Sb-doped SnO_2 samples stabilizes a Sb^{III}/Sb^{V} of a ratio about 1 to 3, and n-conductivity only develops after this stage (Table 1-2).

Table 1-2: Relative amount of Sb^{III} and Sb^{V} determined from the Sb L_1-edge XANES spectra.[26]

Oxidation state and relative amount of antimony chloride employed in synthesis		Preparation conditions	
		Drying at 100 °C Percentage Sb^{III}/Sb^{V}	Drying and subsequent annealing at 500 °C Percentage Sb^{III}/Sb^{V}
9.1% Sb^{III}	(a) after 1 week at 20 °C	35/65	28/72
	(b) after 6 months at 20 °C	22/78	28/72
16.7% Sb^{III}	(c) after 1 week at 20 °C	50/50	23/77
	(d) after 6 months at 20 °C	21/79	21/79
16.7% Sb^{V}	(e) after 1 week at 20 °C	9/91	24/76

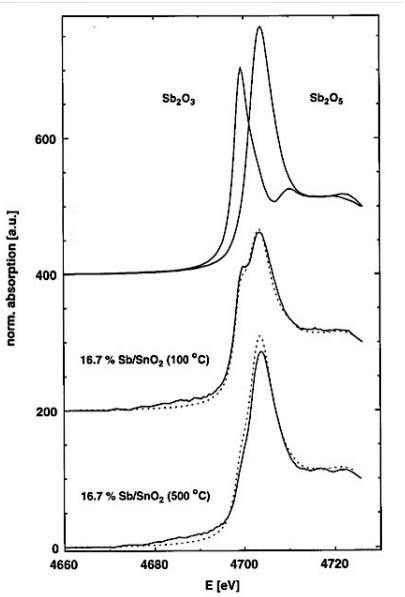

Figure 1-4: Normalized XANES spectra at Sb L_1 edge for references (upper level) and experimental samples after annealing at different temperatures (lower level). Dotted line is the linear combination fit for evaluating Sb^{III}/Sb^{V} ratio.[26]

In 1997, Davis *et al.*[27] used EXAFS to probe incorporation of Cu^{2+} and Fe^{3+} into SnO_2 lattice with the size 2-3 nm and showed that dopants are located on the Sn^{4+} sites. Heating caused a distinct change in the EXAFS interpreted as moving of the dopants to the surface of the nanocrystallites. In the case of a 10 %mol Fe^{3+} doped sample, precipitation of iron oxide has been observed after heating at 900 °C for one hour (Figure 1-5).

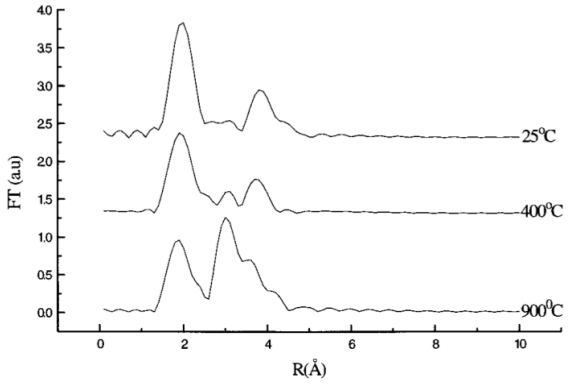

Figure 1-5: Fourier transforms of nominally 10 mol% of Fe-doped SnO_2 for 1h at high temperatures.[27]

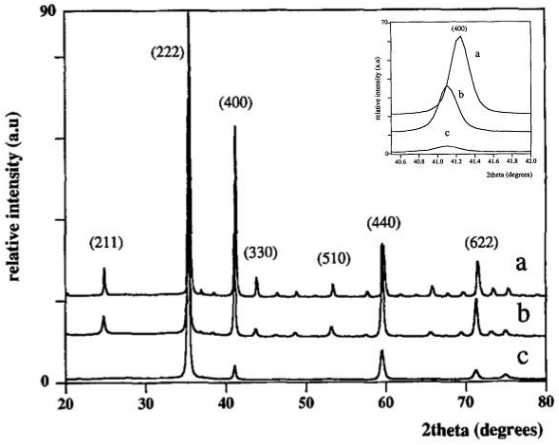

Figure 1-6: Evolution of XRD pattern for (a) undoped In_2O_3 (b) 10% and (c) 39% Sn-doped In_2O_3. The inset is the (400) reflection for the same samples.[28]

In the case of In_2O_3, EXAFS investigations at the In K edge reveal that even in low dopant (Sn) concentration regime, first the oxygen polyhedron and In-In coordination shell are distorted. Distortion will increase by increasing the dopant concentration in Sn-doped In_2O_3, and for a large tin concentration (39%) the In-O shell is locally similar to the high-pressure phase of In_2O_3. Although the structural disorder in Sn-doped In_2O_3 has been proved by X-ray diffraction measurement, distortion induces damping of X-ray reflections (i.e., the network is still ordered within large domains)(Figure 1-6).[28]

Based on crystallographic data, the average In-O bond distances in cubic and rhombohedral are almost the same, and the difference comes from the In-In bond length and coordination number. In the rhombohedral In_2O_3, the In-In distance is 3.243 Å with coordination number 3, while in cubic, the In-In distance and coordination number are 3.35 Å and 6, respectively. Farvid *et al.*[29] have used this information to study phase transformation in pure In_2O_3 nanocrystals thorough EXAFS analysis. They have observed expansion of In-O and In-In distances as the reaction proceeds (Table 1-3) and the increase in In-In distance has been attributed to the phase transformation form rhombohedral to cubic In_2O_3. The conclusion is consistent with the reduction of surface stress due to increase in the size of the nanocrystals during the phase transformation that causes the increase in the In-O bond distance.

Table 1-3: Fitting parameter for the EXAFS analysis of pure In_2O_3 nanocrystals synthesized at 250°C.[29]

	In–O			In–In_1			
t (min)	N	R (Å)	σ^{2a} (Å^2)	N	R (Å)	σ^2 (Å^2)	ρ^b (%)
5	6.0	2.163	0.007	3.3	3.329	0.010	0.6
10	6.0	2.161	0.062	3.8	3.331	0.012	0.6
20	6.0	2.165	0.007	3.2	3.332	0.009	0.5
45	6.0	2.167	0.006	5.1	3.341	0.008	1.3
60	6.0	2.168	0.005	5.9	3.340	0.008	2.0
1800	6.0	2.179	0.006	6.0	3.342	0.005	2.5

[a]Debye–Waller factor. [b]Weighted residual factor.

1.2.2 Magnetic Properties

As discussed in section 1.1, a DMSO material is referred to a semiconductor like ZnO, SnO_2, TiO_2 etc., in which the conventional host lattice is intentionally doped with a magnetic impurity, usually a transition metal (TM) ion, and the resulting material exhibits magnetic ordering, specially ferromagnetism. An important step towards this technology is to explore semiconductor materials that display electrically tunable ferromagnetism above room temperature. Most extensive exploration in this field has been done on ZnO and TiO_2, which are n-type, wide band gap metal oxides.

The first signs of room temperature ferromagnetism were observed on epitaxial $Zn_{1-x}Mn_xO$ ($x<0.35$) thin film.[30] In 2001, the observation of ferromagnetism in dilute Co-doped anatase TiO_2 ($x<8\%$) catalyzed the research on DMSO systems. Matsumoto and co-workers showed that magnetic domain structure that is an indication of ferromagnetic long range ordering remaining above room temperature with magnetic moment of 0.32 μ_B/Co.[31] Since then, intense effort has been done on these as well as other oxides and different dopants seeking for deeper insight for robust ferromagnetism in DMSOs. Ogale *et al.*[32] not only observed ferromagnetism in $Sn_{0.95}Co_{0.05}O_2$ thin film with a curie temperature close to 650 K, but also the magnetic moment per Co atom is 7.5±0.5 μ_B. This "giant" magnetic moment is much larger than the magnetic moment of cobalt metal or small cobalt clusters, 1.67 μ_B/Co and 2.1 μ_B/Co, respectively. The authors have proposed two possibilities for this process: either atoms surrounding Co atom acquired their magnetic moment through electronic correlations or the orbital moment of the cobalt atom has not been quenched for reason that is unclear. The Gamelin group has studied Ni^{2+} incorporated into SnO_2 nanoparticles and a robust ferromagnetism with

saturation moment of 0.8 μ_B/Ni^{2+} has been observed at 300 K. Archer[33] has concluded that the interfacial oxygen vacancies (V_O^{2-}) diffusion has the main contribution in the observed RT ferromagnetism. However, a few percent of magnetic dopant is not sufficient to establish the conventional super-exchange and double-exchange interactions. Thus, the origin of ferromagnetism in DMSO materials is still under debate.

Ferromagnetic exchange coupling has been discussed by Coey *et al*.[34] The authors have proposed that shallow donor electrons (e.g., oxygen vacancy) form magnetic polarons that mediate long range magnetic ordering in these materials. For oxides, he has presented the general formula $(A_{1-x}M_x)(O\square_\delta)_n$ where A is non-magnetic cation that is partially replaced with magnetic cation M, $\square_\delta$ is donor defect and n=1 or 2. Electron associated with a certain defect is confined in a sphere of radius $r_H = \varepsilon(\frac{m}{m^*})a_0$ where ε is dielectric constant, m is mass of electron, m^* is the effective mass of donor electrons (e.g., oxygen vacancy) and a_0 is the Bohr radius. Increasing donor concentration above the critical concentration $n_\square^{crit}$, the localized impurity band states turn to delocalized and the 1s orbitals, $\psi(r) = (\pi r_H^3)^{-1/2}\exp(-r/r_H)$, overlap. A hybridized state can be formed through interaction

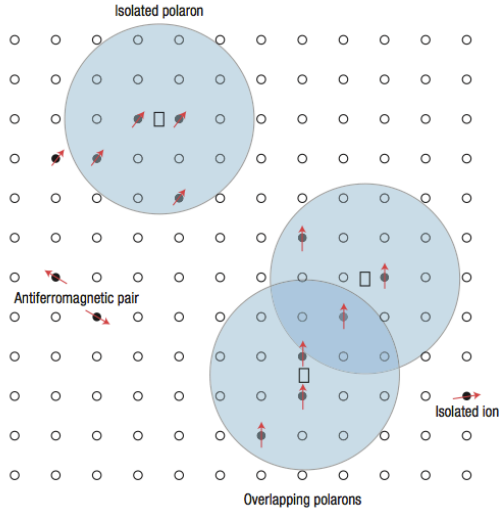

Figure 1-7: Representation of magnetic polarons. A donor electron couples with its spin antiparallel to impurities band with a half-full (or more than half-full) *3d* shell. The figure is drawn for x = 0.1, γ= 12. Small circles represent cation sites, Oxygen is not shown; and the unoccupied oxygen sites are represented by squares.[34]

electronic state of the localized *3d* impurity band, below the cation percolation threshold, and delocalized donor state (Figure 1-7).

In the nanoscale regime, interfacial defects can mediate an inter-dopant coupling mechanism, which increases the magnetic domain volumes, and generates charge carriers through formation of interfacial defects. The role of defects and especially surface defects in mediating long range magnetic ordering in dilute magnetic semiconductors has been addressed in the literatures, which implies the importance of investigating nanostructured materials with high surface to volume ratio.

1.3 Motivations and Scope of the Thesis

Majority of the theoretical and experimental research on diluted magnetic semiconductor oxides (DMSOs) that started in the early 90s has focused on some important areas: microscopic origin and primary nature of ferromagnetism with low dopant concentration at room temperature and structural information of synthesized materials during the growth procedure and influence of defects.

Manganese ions in doped semiconductors have the potential of existence in multiple coordination states, and exploration of electronic structure of Mn doped semiconductors can help to understand the origin and mechanism of magnetic interactions in DMSOs. The precise location of the dopant inside the host lattice, electronic environment around the dopant (octahedral or tetrahedral) and determination of dopant oxidation state are the first pieces of information needed to understand the role of dopant in modifying magnetic properties of diluted magnetic semiconductors oxides (DMSOs). X-ray absorption spectroscopy (XAS) including X-ray absorption near edge structure (XANES) and extended X-ray absorption fine structure is a powerful technique, which provides details of how X-rays are absorbed by an atom at energies near and above binding energy of the absorbent. XAS spectra are sensitive to formal oxidation state, bond distances to the next nearest neighbors, and coordination number of the absorbent. We have applied these techniques to probe the electronic structure of Mn-doped SnO_2 and Mn-doped In_2O_3 nanocrystals. In addition, a combination of structural and spectroscopic methods including XRD, TEM, MCD and ligand field electronic absorption have been used to provide a direct connection between manganese dopant ion separation (location and electronic structure) the desired n-type semiconductors and magnetic properties nanocrystalline film fabricated from free-standing Mn-doped SnO_2 and Mn-doped In_2O_3 nanocrystals.

Magnetic properties of Mn:SnO_2 and Mn:In_2O_3 nanocrystals have been studied using physical property measurement system (PPMS). Investigation of paramagnetic behavior in manganese doped tin oxide and indium oxide nanoparticles and ferromagnetic ordering after film preparation via spin coating has been done to establish the influence of extended interfacial structural defects ion long-range magnetic ordering.

Chapter 2
Experimental Section

2.1 Materials

All commercial reagents and solvents were used as received without further purification. Indium acetylacetonate ($In(acac)_3$; 98%) and tin(IV) chloride pentahydrate ($SnCl_4.5H_2O$, 98%) were purchased from Strem Chemicals. Manganese acetylacetonate ($Mn(acac)_3$) was purchased from Alfa Aesar. Manganese (II) choloride, anhydrous ($MnCl_2$, 97%) was purchased from Strem Chemicals. Oleylamine (70%) and tri-n-octylphosphine oxide (TOPO; 90%) were purchased from Sigma-Aldrich Company. Toluene (99.98%, EMD Chemicals), ammonium hydroxide (30%, Chemicals), hexane (99.9%, Fischer Scientific) and absolute ethanol were used as solvents.

2.2 Synthesis and Samples Preparation

2.2.1 Synthesis of Manganese doped SnO_2 NCs

Mn:SnO_2 nanocrystals (NCs) were prepared in our group via hydrolysis method.[35] In a typical preparation, 1.400 g of $SnCl_4.5H_2O$ and varying amount of manganese precursor ($MnCl_2$ for doping with Mn^{2+} and $Mn(acac)_3$ for doping with Mn^{3+}) were added to 20 mL of de-ionized water. The solution was stirred until the entire precursor was dissolved. After that, the reaction flask was transferred to an ice bath where it sat for at least for 15 minutes. While the flask was still in an ice bath the nucleation of particles was catalyzed with drop wise addition of concentrated NH_4OH until pH 6 was reached. The reaction flask was allowed to settle overnight. The next stage was cleaning the surface of the particles: the crystals were washed with water and centrifuged six times until the absence of manganese ions was confirmed through clear supernatant after the addition of $AgNO_3$. The washed crystals were allowed to settle overnight after re-suspending washed NCs in a solution of dilute NH_4OH, keeping the temperature at 90 °C. It has been shown that any residual dopants on the surface of nanocrystals will be cleaned, and the NCs can be resuspended in nonpolar solvents like toluene or hexane by heating in tri-n-octylphosphine oxide (TOPO) [36] at 140 °C for 1h. The resultant TOPO-capped NCs were precipitated and washed with ethanol. The TOPO treatment was repeated 3 times to guarantee the removal of all surface-bound dopant ions.

2.2.2 Synthesis of Manganese Doped In_2O_3 NCs

Mn-doped In_2O_3 nanocrystals have been synthesized in our group using a single step procedure that has been reported previously.[37-40] 4 mmol of $In(acac)_3$, 48 mmol of oleylamine and varying amount of manganese precursor ($MnCl_2$ for doping with Mn^{2+} and $Mn(acac)_3$ for doping with Mn^{3+}) were mixed in 100 mL three-neck round-bottom flask. The mixture was degassed, heated to 250 °C and allowed to proceed in Ar atmosphere for at least 1 h under constant stirring. After cooling the solution to room temperature, Mn-doped In_2O_3 was collected by washing with ethanol and centrifugation. Mn-doped In_2O_3 with larger size has bixbyite structure while smaller NCs exhibit rhombohedral structure. So, size selective precipitation can be applied to separate rh-In_2O_3 and bcc-In_2O_3. In this method, colloidal suspension centrifuged at 3000 rpm for 5 min. Large bixbyite In_2O_3 precipitated at bottom and supernatant included small rhombohedral In_2O_3. For precipitating the rh-In_2O_3 NCs, 20 mL of ethanol was added and centrifuged for at least 10 min at 3000 rpm. All precipitated NCs were melted in TOPO, followed by precipitation with ethanol. This process repeated 3 times to clean all bound dopant from the surface.

2.3 Measurement and Data Analysis

2.3.1 Electron Microscopy

Transmission electron microscopy (TEM) was performed with a JEOL-2010F microscope operating at 200 kV. For sample preparation, samples were diluted in toluene and multiple drops of dilute suspensions placed on standard copper grids with lacey formvar/carbon support films purchased from Ted Pella, Inc. microstructure measurement software was used to determine the size of NCs.

2.3.2 Powder X-Ray Diffraction

Powder X-ray diffraction (XRD) is a rapid analytical technique for identification of the crystal structure of materials, and it can be used to determine the unit cell parameters of the crystal. In addition to defining the crystal structure of the material, crystallite size also can be determined through Debye-Scherrer formula:

$$T = \frac{C\lambda}{B\cos(\theta)} \qquad \text{Equation 2-1}$$

Where T is the crystallite thickness, C is a dimensionless shape factor with a value close to unity, λ is the wavelength of the X-ray radiation (1.5418 Å), B is the full width at half maximum (FWHM), and finally θ the is diffraction angle in radians.

Powder X-ray diffraction (XRD) patterns were recorded in an INEL diffractometer equipped with a position-sensitive detector, using monochromatic Cu-Kα radiation. For XRD measurement, precipitated samples were dried and loaded as powder on aluminum XRD sample holder.

2.3.3 X-Ray Absorption Spectroscopy (XAS)

Extended X-ray absorption fine structure (EXAFS) is a unique technique that is capable of studying the local structure around a selected atom at the atomic level. The application of EXAFS has not been limited to crystalline materials, and materials with little or no long-range translational order can be studied as well. In this technique, the X-ray absorption coefficient, μ(E), is measured as a function of energy and describes how strongly an x-ray would be absorbed by the material in different energies.

For a sample that absorbs the monochromatic synchrotron radiation, the absorption coefficient can be deducted according to absorption law:

$$\mu(\mathrm{E}) = \ln(\frac{I_0}{I}) \qquad \text{Equation 2-2}$$

where I_0 and I are the incident and transmitted beam, respectively. The absorption cross-section, which is proportional to μ(E) has been depicted in Figure 2-1.

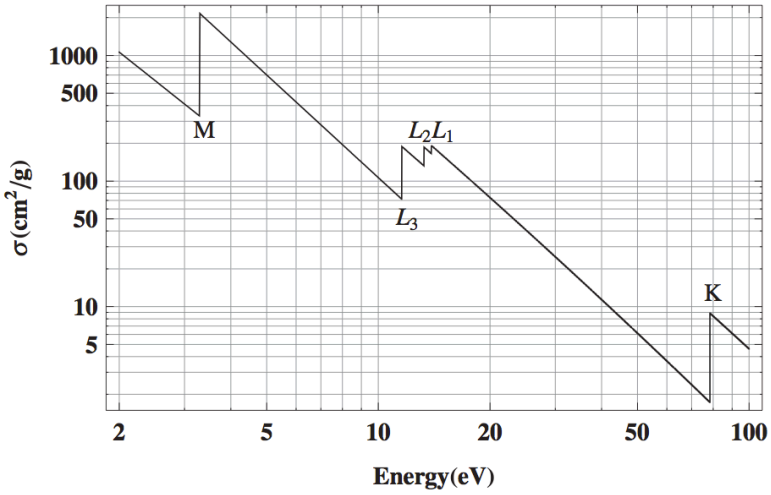

Figure 2-1: Log-log plot of the X-ray absorption cross-section for Platinum (Z=78) as a function of energy.[41] The individual absorption edges are marked as M, L and K edges.

As is evidenced in Figure 2-1, at low energy, increasing in the energy of the incident beam causes the reduction of the absorption coefficient. This region is named the pre-edge. The pre-edge structure of, say, a K-edge, is where the electron in the K-shell (1s) is promoted to another unoccupied level, rather than being removed. The second feature in the absorption cross section is the step increase, which is named the absorption edge, happening at certain energies. In this region, the energy of the X-ray beam is sufficient for the ionization of the atom, and sending the electron from the corresponded shell (K, L, M etc.) to the continuum energy state (Figure 2-2). So, this step is the difference between the energy of the core level and Fermi level. This energy range, which is called

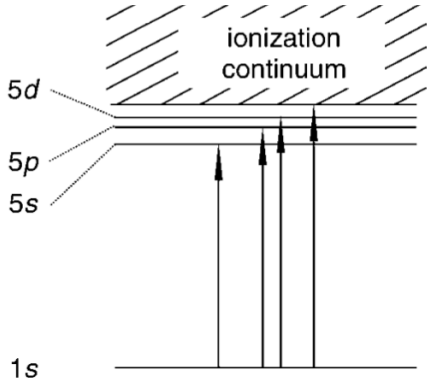

Figure 2-2: Formation of absorption edge and pre-edge structure in X-ray absorption.

X-ray absorption near edge structure (XANES), leads to a more or less complex in absorption edge. The last feature that happens at high energies corresponds to extended X-ray absorption fine structure (EXAFS). Excitation of core electron by the X-ray photon, leads to formation of excited photoelectrons with a nonzero kinetic energy, which propagate through the material. The forward propagating wave, associated with the photoelectrons, scatters from the surrounding atoms and the interference between the forward and backscattered waves results in formation of the modulations of the measured absorption coefficient (Figure 2-3).

Analysis of the EXAFS spectra can provide information about the structural parameters for the absorbent e.g. coordination number, bond distances and Debye-Waller factor. The first step in analyzing the EXAFS area is to remove the absorption edge and possible background from the spectrum. The function that describes the EXAFS region can be expressed as:

$$\chi(\mathrm{E}) = \frac{\mu(\mathrm{E}) - \mu_1(\mathrm{E})}{\mu_1(\mathrm{E}) - \mu_0(\mathrm{E})} \qquad \text{Equation 2-3}$$

Where μ is the experimental absorption coefficient, E_0 is the absorption edge energy; $\mu_1(\mathrm{E}) - \mu_0(\mathrm{E})$ is the step edge at absorption and μ_1 is the free atomic background that is attributed to oscillation free absorption. Fourier transform of the EXAFS $\chi(\mathrm{k})$ will give the radial distribution function, which can be used in a best-fit procedure to explore information on distances and type of the surrounding atoms or ions.

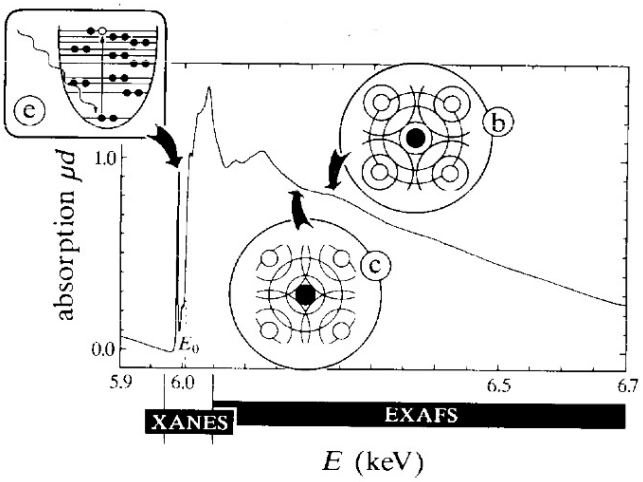

Figure 2-3 Interference of the photoelectrons in the crystal lattice for Cr K edge in K_2CrO_4.[42]

XAS measurements were performed at the beamline 06ID-1 at the Canadian Light Source (CLS). For Mn K-edge the energy was scanned in the range of 6300-8203 eV. The scan started from 250 eV below the edge (for chromium at 5989 eV) to 50 eV below the edge in 10 eV steps. Between 50 eV below the edge and 50 eV above the edge, the step size was 0.2 eV. Above 50 eV of the edge the step size was 0.05 Å-1 until the end of the scan was reached at 15k (where $k = \sqrt[2]{0.2625\ (E - E_0)}$).

2.3.4 UV-Vis Absorption Spectroscopy

Ultraviolet visible (UV-Vis) spectroscopy refers to absorption spectroscopy in the ultraviolet-visible region. Electronic absorption spectroscopy has an important effect on the development of methods for synthesizing pure semiconductor nanocrystals. This technique has provided valuable information about nanocrystal size, size distributions, growth kinetics, growth mechanism and electronic structure of semiconductors.

Doped semiconductors exhibit more features on absorption spectra. The main features are visible in spectra and can be listed in three categories; (I) the valence to conduction band transition (band gap) of the semiconductor, (II) internal transitions of the dopant ions in the lattice which include ligand field or d-d transitions, and (III) charge transfer transitions in which a large fraction of an electronic charge density transfers from the dopant electrons to the conduction band or from valence band of the semiconductors into dopant-localized orbital. The information from each of these transitions carries a better insight about the local coordination environment around the dopant ion in the host lattice. As an illustration, consider a metal ion at the center of an octahedral complex. According to crystal field theory, the ligand repels the electrons in the d orbital of the central metal ion. The Cartesian coordination can be used to depict the six ligands in an octahedral complex. Those d orbitals with high electron density near the ligand would be repelled by the ligand to the maximum extent and would have higher energies. Therefore, the five degenerate d orbitals will split to high-energy $d_{x^2-y^2}$ and d_{z^2} (e_g) orbitals and low energy d_{xy}, d_{yz} and d_{xz} (t_{2g}) orbitals[43] (Figure 2-4). The energy difference between these two sets is termed crystal field splitting energy (Figure 2-4).

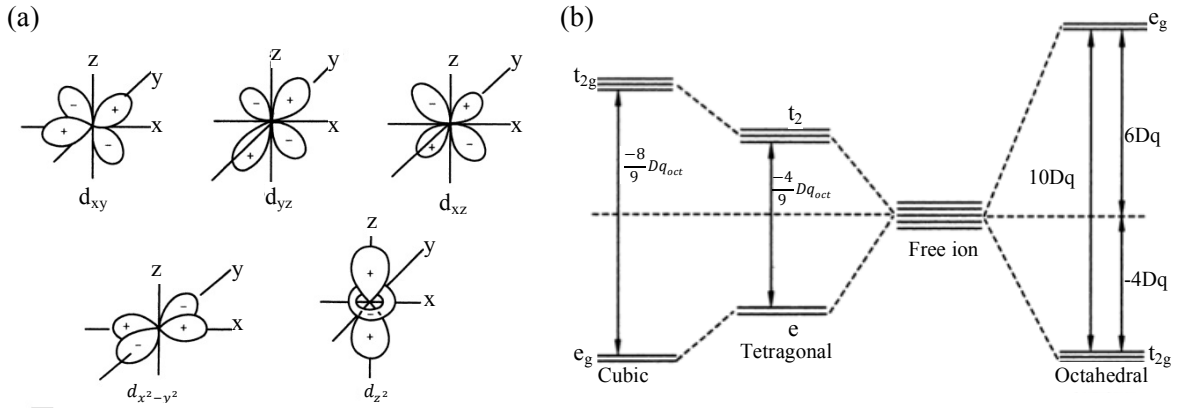

Figure 2-4: (a) shape of d orbitals, (b) the d orbital splitting in cubic, tetrahedral and octahedral crystal field.[43]

Optical absorption spectra were collected with Varian Cary 5000 ultraviolet/visible/near-infrared (UV/vis/NIR) spectrophotometer using 1 cm path-length quartz cuvettes.

2.3.5 Magnetic circular dichroism (MCD)

The differential absorption of the left circularly polarized (LCP) and right circularly polarized (RCP) light, which is induced in a sample by a strong magnetic field, is the fundamental strategy in magnetic circular dichroism (MCD) spectroscopy. Strong magnetic field is responsible for Zeeman splitting of the ground state and excited state involved in optical transition (Figure 2-5). The difference in absorption is defined as $\Delta A = A_- - A_+$, where A_- and A_+ are lcp and rcp absorptions, respectively.

Although MCD and UV-Vs absorption measurements follow the same fundamentals, but MCD spectra shows improved resolution compared to absorption measurement. Typically, if $\frac{\Delta A}{A} > 10^{-2}$, then the transitions are only visible in MCD measurement rather than optical absorption. Moreover, weak transitions that are concealed under a stronger transition can appear in MCD spectra. Additionally, a variation of applied field and temperature provides the path to better insight about electronic excited state properties, nature of transitions (metal d-d and charge transfer (CT) transition), and ground state magnetic properties (Lande g-factor, spin state, zero-field splitting and magnetic coupling).

MCD spectra were measured with Jasco J-815 spectropolarimeter using a high-field superconducting magneto-optical cryostat (SM4000-8, Oxford) with a variable-temperature (1.5-300

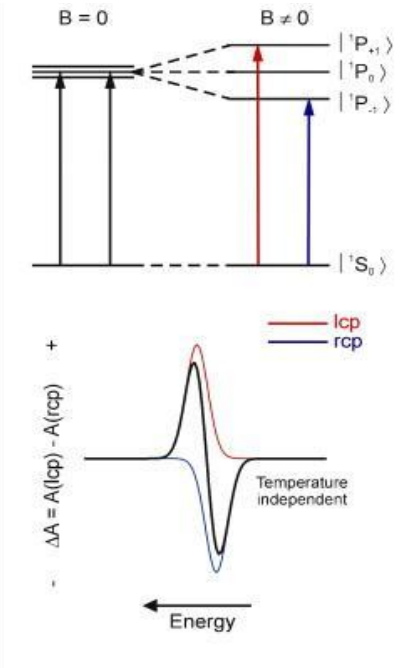

Figure 2-5: (a) Schematic representation of energy levels showing non-degenerate $|\,^1S\rangle$ and orbitally degenerate $|\,^1P\rangle$ states.[44]

K) and variable magnetic field (0-8 T) compartment positioned in the Faraday configuration. For MCD measurements, the colloidal suspensions were deposited on high quality quartz disks and mounted in the appropriate cryostats.

2.3.6 Magnetic Measurements

The magnetization was measured with the physical property measurement system (PPMS, Quantum Design) in ACMS mode, with helium cooling system, allowing a wide range of temperatures from 2 to 400 K and magnetic fields up to ± 9 Tesla. The overall effective magnetic moment can be measured as a function of temperature, or the applied magnetic field from a positive to a negative one, while monitoring magnetic properties. For magnetization measurement, samples were prepared as nanocrystalline film via spin coating: the colloidal NCs were spin-coated multiple times on the clean

sapphire substrates, followed by mild annealing at 300 °C for 1 minute between consecutive coatings (Figure 2-6). The final nanocrystalline films were weighed again on an analytical balance in order to determine the magnetization per unit mass of the samples. All samples were handled identically under

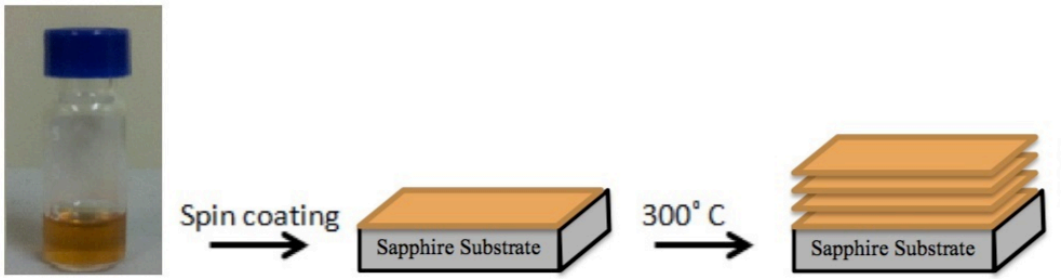

Figure 2-6: Schematic representation of preparation of films from colloidal Mn:SnO_2 NCs for magnetic measurements.

carefully controlled magnetic contamination-free conditions. For each sample, three to five films were prepared. Although the magnetic moment varies, the data were generally in good agreement from one film to another. The saturation magnetization per dopant ion in the nanocrystalline film was estimated based on the unit mass magnetization of the sample.

Chapter 3

Structural Analysis of Mn-Doped SnO_2

In this part of my thesis we synthesized and performed the structural analysis of Mn-doped SnO_2 nanostructures (nanocrystals and nanowires) In this chapter we first review a combination of structural and spectroscopic methods, including TEM, XRD, UV-Vis to get insight about the size and crystal structure of tin oxide NCs. Then, a detailed structural analysis has been carried out using XANES and EXAFS spectroscopy, for a better understanding about the environment around the dopant.

3.1 Review of Tin Oxide Properties

Transmission electron microscopy (TEM) micrographs were used to investigate the morphology of the synthesized Mn-doped tin oxide nanocrystals. As shown in Figure 3-1, the nanocrystals with a quasi-spherical shape are well dispersed in the solution. The inset, lattice-resolved image (Figure 3-1) of isolated nanocrystals emphasizes that the particles are single crystals with average d-spacing

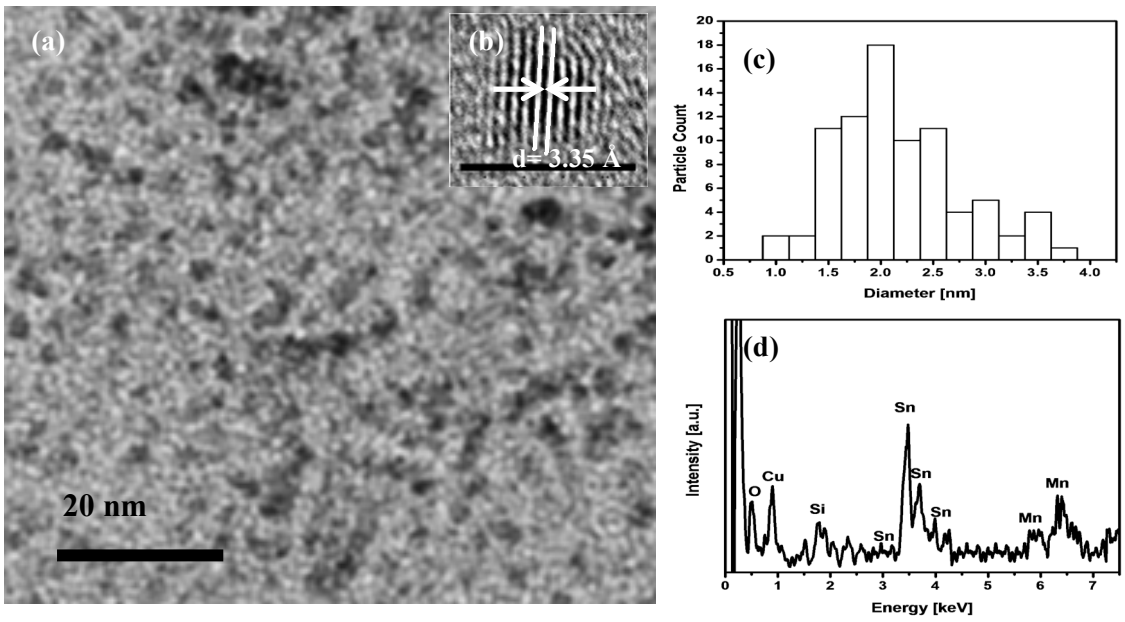

Figure 3-1: (a) TEM image of nanocrystalline Mn-doped SnO_2, (b) high-resolution TEM image of the same sample. The scale bar is 5 nm, (c) size distribution histogram of the corresponding Mn-doped SnO_2 nanocrystals with 10% starting dopant concentration (d) EDX profile of the Mn-doped SnO_2.[45]

d = 3.35 Å, which corresponds to the rutile SnO_2 in the direction of {110} planes. The corresponding size distribution histogram is depicted in Figure 3-1. In the graph the synthesized nanoparticles fall in a narrow size distribution with the average diameter of about 2.3 nm. Figure 3-1 confirms the incorporation of manganese in the tin oxide lattice with the 10% starting concentration of $MnCl_2$ precursor ($\frac{[Mn]}{[Mn+Sn]}$), using energy dispersive X-ray (EDX) spectroscopy.

X-ray diffraction (XRD) patterns of pure and Mn-doped SnO_2 nanocrystals prepared with different manganese concentrations are shown in Figure 3-2. All the diffraction peaks can be readily indexed to the cassiterite crystal structure with space group $P4_2/mnm$, according to the JCPDS file No. 41-1445. From the X-ray crystallographic data, no sign of major structural changes upon adding of dopant has been observed.

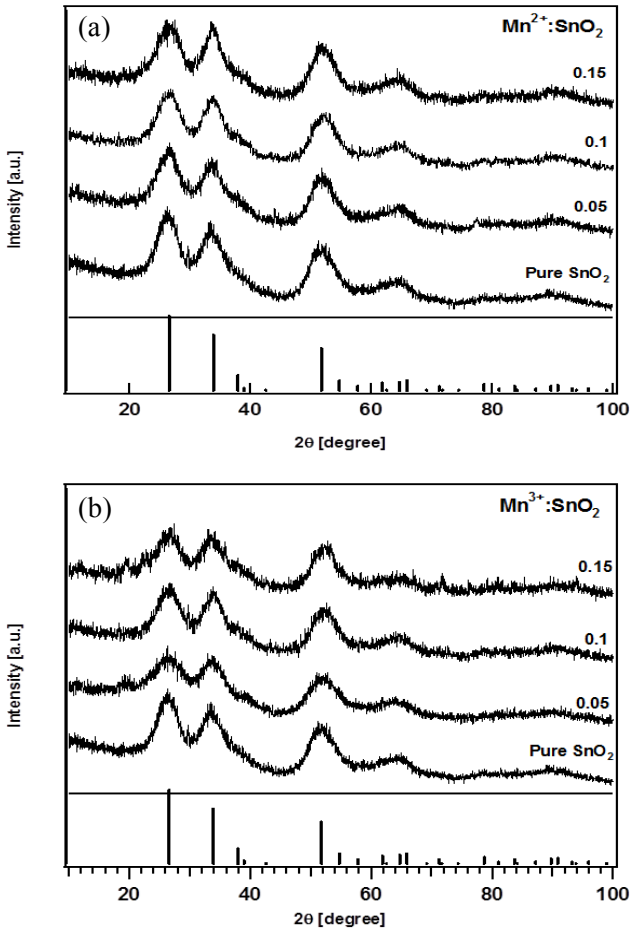

Figure 3-2: XRD patterns for SnO_2 doped with different concentrations of (a) $MnCl_2$ and (b) $Mn(acac)_3$.The vertical lines at the bottom are the representative pattern for the bulk rutile SnO_2.

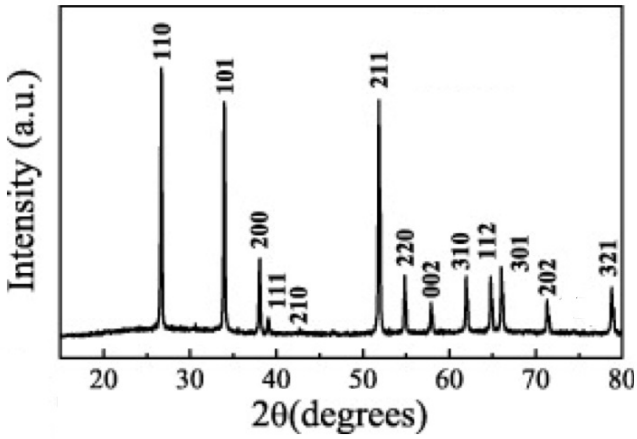

Figure 3-3: XRD pattern of bulk SnO_2.[46]

Apparently, the increase in dopant concentration does not show a pronounced effect on the size of Mn-doped SnO_2 nanocrystals. Compared to the bulk rutile tin oxide, Figure 3-3, Mn-doped SnO_2 exhibits broader peaks, and the full width at half maximum (FWHM) has been decreased that indicates the nanosized nature of Mn-doped SnO_2 particles, as confirmed by HRTEM in Figure 3-1. Crystallite sizes correspond to the most pronounce diffraction peak, (110), has been calculated using Debye-Scherre's equation:[47, 48]

$$T = \frac{C\lambda}{B\cos(\theta)}$$

Table 3-1 summarizes the results for crystallites size. As evidenced by TEM images, the nanocrystals are well dispersed and the average size of crystallite should be the same as nanoparticle size. The grain size of cassiterite phase is determined to be 2.1-2.6 nm, which is in a very good agreement with size distribution histogram extracted from TEM micrographs.

Table 3-1: Crystallite size of Mn-doped SnO_2 with different dopant concentration.

	Pure SnO_2	$Mn^{2+}:SnO_2$ 5%	$Mn^{2+}:SnO_2$ 10%	$Mn^{2+}:SnO_2$ 15%	$Mn^{3+}:SnO_2$ 5%	$Mn^{3+}:SnO_2$ 10%	$Mn^{3+}:SnO_2$ 15%
Full Width at Half Maximum (θ)	4.264	4.125	4.160	4.140	5.648	4.158	4.839
Average Size (nm)	2.37	2.42	2.40	2.40	2.17	2.40	2.57

3.2 Manganese K-edge Measurement

The degree of oxidation of a specific atom in a chemical compound can be represented through its oxidation state number. X-ray absorption near edge spectroscopy (XANES) allows for identification of the valence state of a selected atomic species in the sample. The symmetry of an unoccupied electron level also affects the shape and energy shift of X-ray absorption edge.[49, 50] The changes in the electronegativity of the neighboring atoms causes a shift in the absorption edge energy, and it has been shown this energy shift observed in the K-edge is proportional to the valence state, according to Kunzl's law.[51, 52] So, in a system with the same ligand type, the least-squire-fitted line can be used to determine the valence state of the absorbing atom.

The first step to quantitatively compare the intensities of K-edge absorption energies of the absorbing atom is to normalize the spectra. This process is graphically shown in Figure 3-4. In the normalization process, the possible background that is the oscillation-free absorption after the edge as well as the absorption jump, which would occur if there would not any absorption edge, should be removed from the rough absorption data:

$$\chi(\mathrm{E}) = \frac{\mu(\mathrm{E}) - \mu_1(\mathrm{E})}{\mu_1(\mathrm{E}) - \mu_0(\mathrm{E})}$$

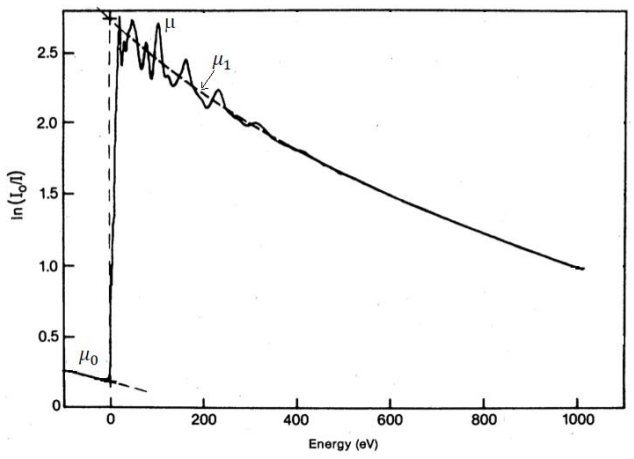

Figure 3-4: Edge-normalization procedure for vanadium (V) K-edge. E_0 is found according to inflection point of the spectrum.[49]

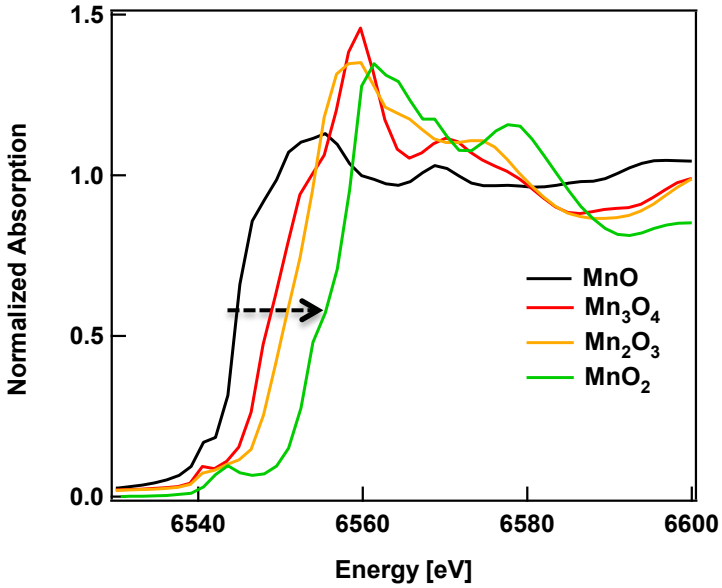

Figure 3-5: XANES spectra of different manganese oxides.

Figure 3-5 shows the normalized XANES spectra, extracted from EXAFS spectra, of manganese oxides studied as references for Mn-doped SnO_2 nanocrystals. When the absorbent e.g. Mn occupies an octahedral site, the centro-symmetry around the atom does not allow any p-d mixing, but quadrupole transitions are allowed, which by the Fermi golden rules would have low transition probability. This leads to very little or even the absence of a pre-edge feature in the XANES spectrum. Distortion of octahedral structure will increase the probability of p-d mixing as well as the quadrupole transitions. So, in a tetrahedral symmetry, a large pre-edge peak will form. Campos *et al.* have presented this argument in the example of Mn substituting tetrahedral and octahedral sites in Fe_3O_4 lattice Figure 3-6.[53]

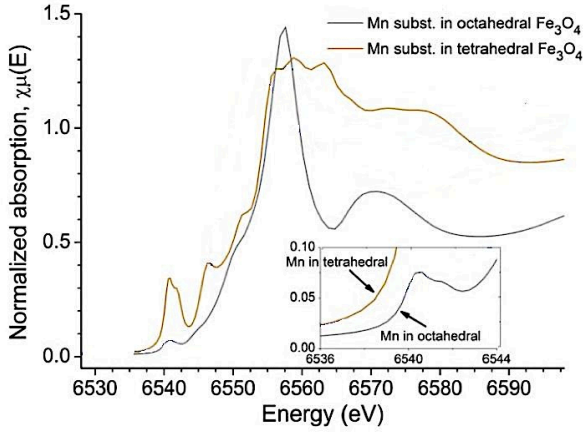

Figure 3-6: Mn K-edge XANES. Mn substitutes Fe^{2+} (tetrahedral) and Fe^{3+} (octahedral) sites in Fe_3O_4 FEFF calculations.[53]

The XANES spectra, Figure 3-5, also show that by increasing the oxidation state from 2+ (MnO) to 4+ (MnO_2) the edges of the spectra shift to higher energies. Figure 3-7 shows the energy of absorption edge vs. oxidation state for different manganese oxides, which follows Kunzl's rule, as discussed before, with $R^2 = 0.9838$ for the fitted line. This means that the oxidation state of any samples can be determined by defining the position of absorption edge.

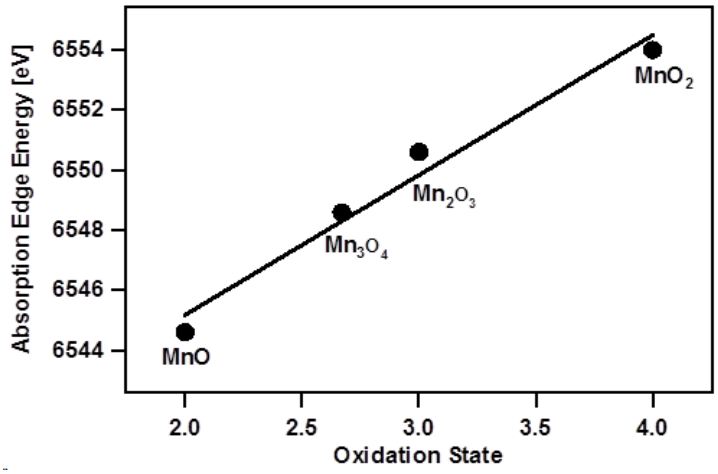

Figure 3-7: Absorption energy vs. oxidation state for different manganese oxides.

The EXAFS spectra are derived for the Mn-O shell by the inverse Fourier transform of Figure 3-8 (a). The Fourier transform transfers the EXAFS oscillations into the real space where the peaks resemble scattering of the photoelectrons from the nearest neighbors, and the first peak that represents the first shell occurs in the range R= 1.23-1.99 Å. Figure 3-8 (a) shows Fourier-filtered EXAFS of different manganese oxides. The dashed lines in Figure 3-8 (a) show the fitting results for calculation of structural parameters.

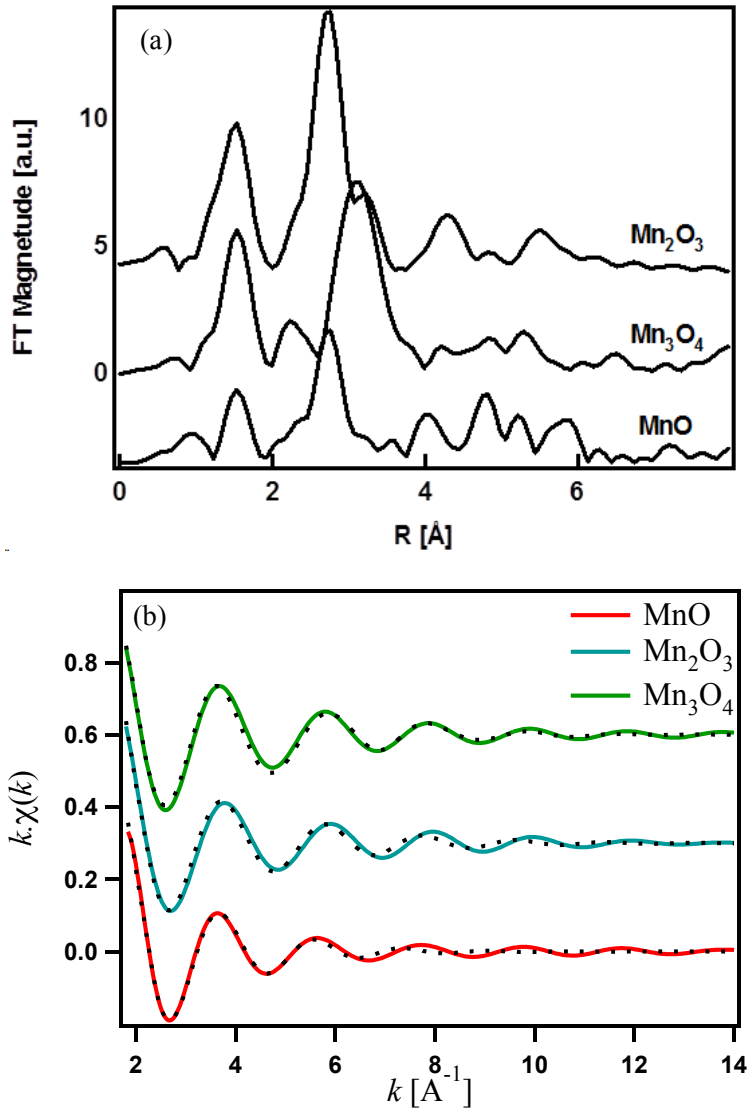

Figure 3-8: (a) Fourier- filtered EXAFS of MnO, Mn_2O_3 and Mn_3O_4 and the resulting curve fits (dashed lines) to calculate the structural parameter, (b) fast Fourier transform into the real space.

According to the literature, MnO has the rock salt crystal structure with space group $Fm\bar{3}m$ and lattice parameter a = 4.4448 Å at 300 K.[52-54, 8] Both cations and anions are octahedrally coordinated and the Mn-O bond distance is 2.222 Å with a high spin ground state $t_{2g}^3 e_g^2$.[54, 55] The cubic lattice of bixbyite Mn_2O_3 includes manganese octahedrally coordinated with oxygen atoms and all 6 Mn-O bond lengths are 1.993 Å. None of the peaks correspond to Mn-Mn distance exists before 3 Å, as is evidenced from Figure 3-8. The space group of Mn_2O_3 is *Ia3* and lattice parameter is a = 9.408 Å. $3d^4$ electrons in the high spin ground state of Mn_2O_3 can be represented as $t_{2g}^3 e_g^1$. In the case of Mn_3O_4, the crystal structure is a distorted spinel with a tetragonal lattice with space group $I4_1/amd$ and lattice parameters a = 5.7691 Å and c = 9.4605 Å. The spinel structure contains two different sites. The divalent Mn^{2+} ions occupy the tetrahedral sites, whereas the Mn^{3+} ions are located at octahedral sites. The normal spinel formula can be represented as $(Mn^{2+})^{tet}(Mn^{3+})_2^{oct}O_4$, which means Mn_3O_4 is a mixture of 1/3 tetrahedral and 2/3 octahedral structures within, raising the total valence number of Mn to 2.67. The MnO_6 octahedra are elongated along [001] due to Jahn-Teller effect. So, the four Mn-O shorter ionic bonds are 1.932 Å and the two longer Mn-O covalent bond lengths are 2.284 Å, while the Mn-O semi-covalent bond distances in the tetrahedral sites are 2.044 Å.[56] Lastly, manganese oxide, MnO_2, crystalizes in a rutile structure, a body-central tetragonal lattice, with $P4_2/mnm$ and lattice parameters a = 4.396 Å and c = 2.871 Å. The Mn atoms have coordination number of 6. Two of Mn-O bond lengths are 1.877 Å and the last four bond lengths are 1.891 Å.

Results for simulated EXAFS spectra of different manganese oxide are summarized in Table 3-2. In contrast with MnO and Mn_2O_3, both octahedral and tetrahedral sites have been considered to obtain more precise fitting results for Mn_3O_4.

Table 3-2: Fitting parameters determined by analyzing EXAFS spectra for different manganese oxides as references.

	Coordination Number (CN)	$R(Mn-O)$ (Å)	σ^2 (Å^2)	ρ
MnO	6	2.20	0.01895	1.812
Mn_2O_3	6	1.99	0.00922	3.28
Mn_3O_4	6	1.82	0.008	1.295
	4	1.99	0.006	

Incorporation of manganese ions inside the SnO_2 host lattice, formation of a secondary phase, and the local environment of Mn in the tin site can be investigated using XANES. Figure 3-9 exhibits Mn K-edge XANES spectra for SnO_2 nanocrystals doped with different concentrations of $MnCl_2$ and $Mn(acac)_3$. For comparison, XANES spectra of manganese oxides with different oxidation states are shown and indicated as reference compounds. The samples spectra are mutually similar, but noticeably different from reference spectra, suggesting the substitutional incorporation of manganese ion inside the tin oxide lattice rather than formation of oxide secondary phase. Absence of pre-edge peak confirms that manganese is exhibiting octahedral features and represents a Centro-symmetry environment in the manganese site. Visual inspection of Figure 3-9 immediately reveals that the absorption edge of Mn-doped SnO_2 NCs shifts to higher energies and lies between the edges of MnO and Mn_2O_3. Hence, it's intuitive that the oxidation state of substituted Mn^{2+} and Mn^{3+} is between 2 and 2.67 and increases with increasing dopant concentration. For a more quantitative determination of Mn oxidation state one can exploit its empirical relation with the absorption edge position by plotting the half-height energy of the normalized spectra vs. oxidation state, using the reference compounds for calibration. It should be noted that the noise contribution with XANES measurements is unavoidable, and careful smoothing of the spectra is needed. If intermediate peaks or pronounced shoulder does not appear in the absorption edge at a μ-value close to 0.5, it's found that the energy edge is reasonably unresponsive to the extent of the smoothing.[57] Figure 3-10 shows, a reasonably good, linear relation between edge energy and oxidation state, according to Kunzl's law. For Mn^{2+}-doped SnO_2, the effective oxidation states range from 2.3+ (for 5% Mn) to 2.5+ (for 15% Mn). Changes in the oxidation state of Mn^{3+}-doped SnO_2 nanocrystals with different concentration are almost negligible. The summary of analyzed data is presented in Table 3-3. It's worth noting that similar results are obtained by inflection point analysis of the spectra.

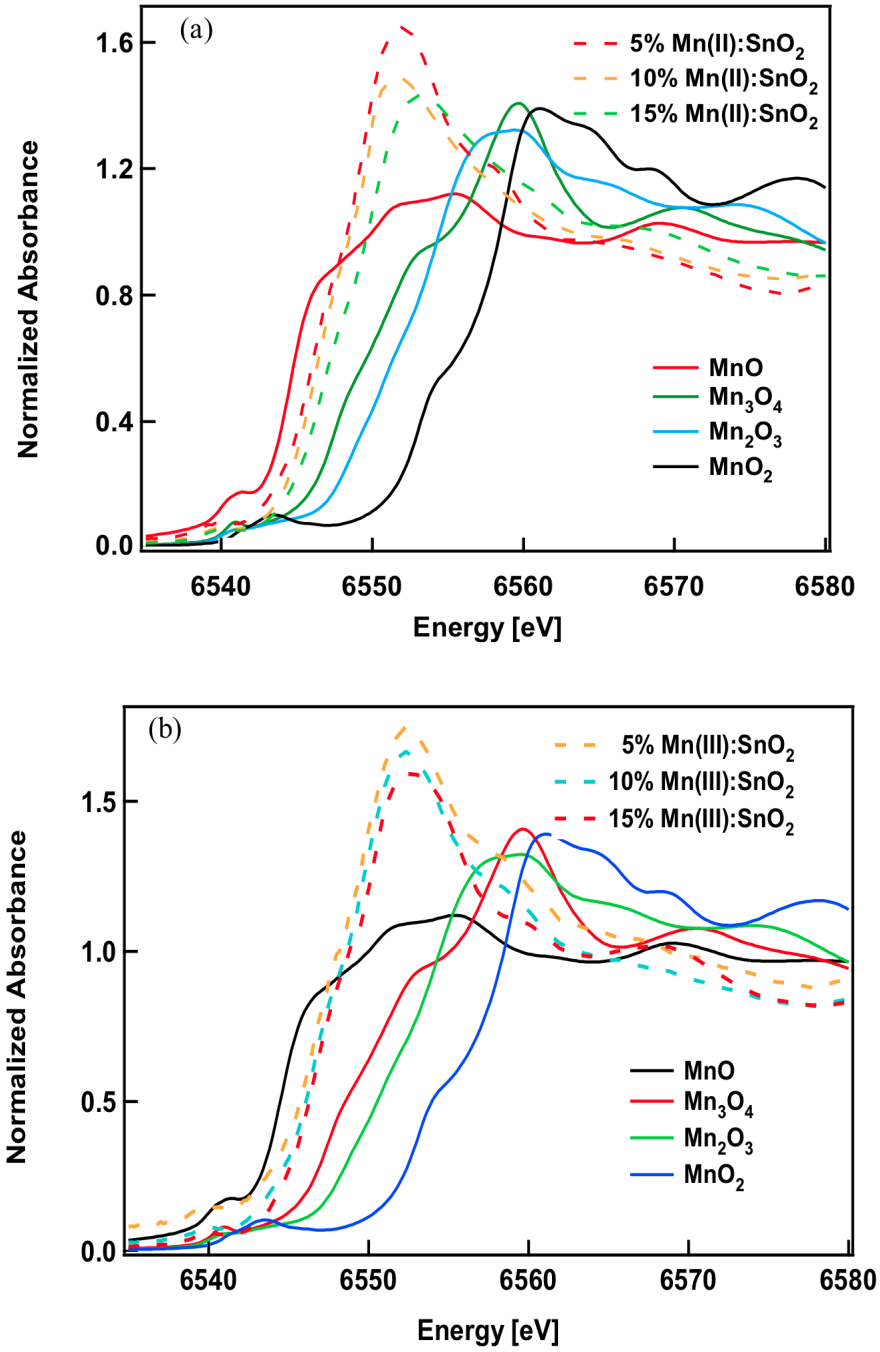

Figure 3-9: Mn K-edge XANES Spectra (a) Mn^{2+}-doped SnO_2 and (b) Mn^{3+}-doped SnO_2 nanocrystals with nominal dopant concentration 5, 10 and 15% and standard manganese oxides.

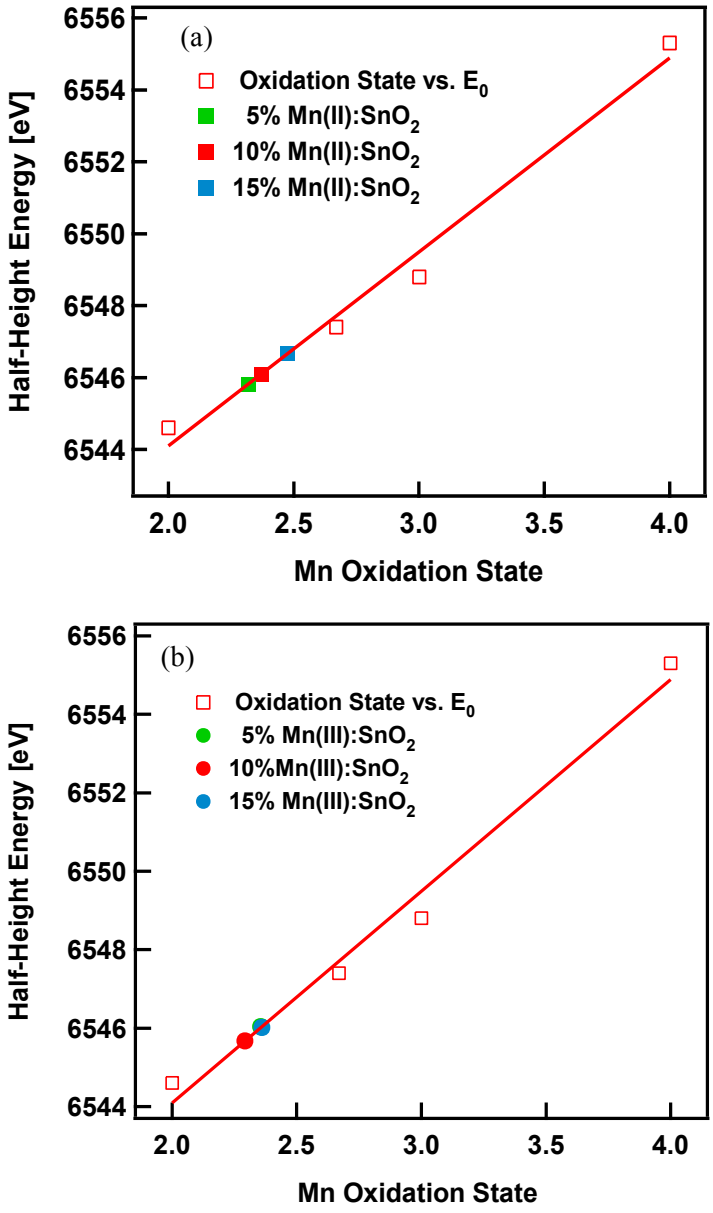

Figure 3-10: Half-height energy of normalized spectra vs. manganese oxidation state for Mn^{2+}- and Mn^{3+}-doped SnO_2 nanocrystals.

Table 3-3: The results for energy edge and Mn oxidation of state for synthesized Mn: SnO_2 NCs Obtained from XANES spectra.

Sample	Dopant Concentration	Energy Edge (eV)	Oxidation State	$\frac{Mn^{2+}}{Mn^{2+}+Mn^{3+}}$ (%)
Mn^{2+}:SnO_2	5%	6545.81	2.31	71.1%
	10%	6546.1	2.37	64.3%
	15%	6546.67	2.47	50.7%
Mn^{3+}:SnO_2	5%	6546.04	2.36	65.6%
	10%	6545.67	2.29	74.4%
	15%	6546.01	2.35	66.3%

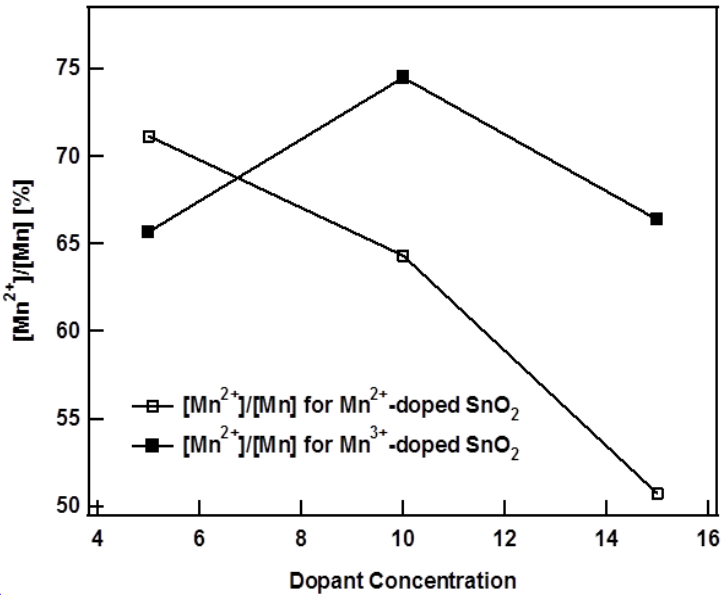

Figure 3-11: Mn^{2+} fraction for the synthesized Mn^{2+}- and Mn^{3+}-doped SnO_2.

Inspection of results for Mn^{2+}-doped SnO_2 imply that, due to oxidative reaction conditions, a significant amount of Mn^{3+}, 36-49%, is observed in the prepared nanocrystals although the precursor that has been used was $MnCl_2$. Presence of Mn^{3+} is also confirmed by optical absorption spectroscopy, which will be discussed later. This situation is even more pronounced for the samples synthesized using $Mn(acac)_3$ as the precursor. In spite of starting with Mn^{3+}, the prepared Mn:SnO_2 nanocrystals ended up displaying dominant Mn^{2+}concentration (65-75%).

To quantitatively investigate the coordination environment of Mn sites, we conducted systematic EXAFS analysis of Mn^{2+}- and Mn^{3+}-doped SnO_2 with different Mn concentration. Normalized Mn K-edge X-ray absorption spectra in the full spectral range for both Mn^{2+}- and Mn^{3+}-doped SnO_2 are shown in Figure 3-12, respectively. Figure 3-12 shows the k-weighted Mn K-edge EXAFS spectra for both Mn^{2+}: SnO_2 and Mn^{3+}: SnO_2. The Fourier transform of the spectra in Figure 3-12 from k-space to R-space is done to yield the pseudo-radial distribution function for Mn^{2+}- and Mn^{3+} in Figure 3-12. Ejected photoelectron from the first coordination shell of neighboring oxygen atoms results in observation of the first peak in the range from ca. R=1.2 – 2 Å and is associated with Mn-O bond distance.

In the R-space, the inverse Fourier transform of the first shell of the pseudo-radial distribution function gives rise to Mn-O Fourier-filtered EXAFS oscillations. Resulting spectra, which are k-weighted are presented in Figure 3-13. The Fourier-filtered curves are fitted in the framework of single scattering theory, using the characteristic parameters of Mn^{2+} (in MnO crystal structure) and Mn^{3+} (in Mn_2O_3 crystal structure), shown as the dashed lines in Figure 3-13 that represent a good agreement with experimental data (solid lines). Figure 3-13 (c) depicts k^3-weighted Fourier-filtered spectra, for 10% Mn^{2+}-doped SnO_2 NCs, to compensate for the decrease in amplitude of oscillations at higher energy regime. Figure 3-13 (c) clearly shows that fitting results considering only Mn^{2+}-O or Mn^{3+}-O distance will not provide a good result, while taking into account both Mn-O distances exhibit a good agreement with experimental data, as shown by the solid line. Fitting parameters including Mn^{2+}-O and Mn^{3+}-O bond distances, Debye-Waller factor (σ^2), and weighted residual factor (ρ) are summarized in Table 3-4. Since the XANES spectra confirm the incorporation of Mn species in the tin site that is octahedral, the number of nearest neighbors (oxygen) atoms is fixed at 6. Considering the ionic radii of Mn^{2+} ($r = 0.83$Å), Mn^{3+} ($r = 0.65$ Å) and Sn^{4+} ($r = 0.69$ Å), the fitting parameters obtained from EXAFS analysis Table 3-4 are consistent with the XANES results. For the Mn^{2+}: SnO_2 nanocrystals, the comparison between Mn^{2+} fraction obtained from XANES analysis in Figure 3-11 and Mn-O bond distances in Table 3-4 implies that the decrease in Mn^{2+} fraction is associated with the decrease in Mn^{2+}-O bond distances exhibiting a clear shrink of the host lattice. This excellent agreement reveals the correlation between doping concentration, electronic structure, dopant oxidation state, and lattice parameters.

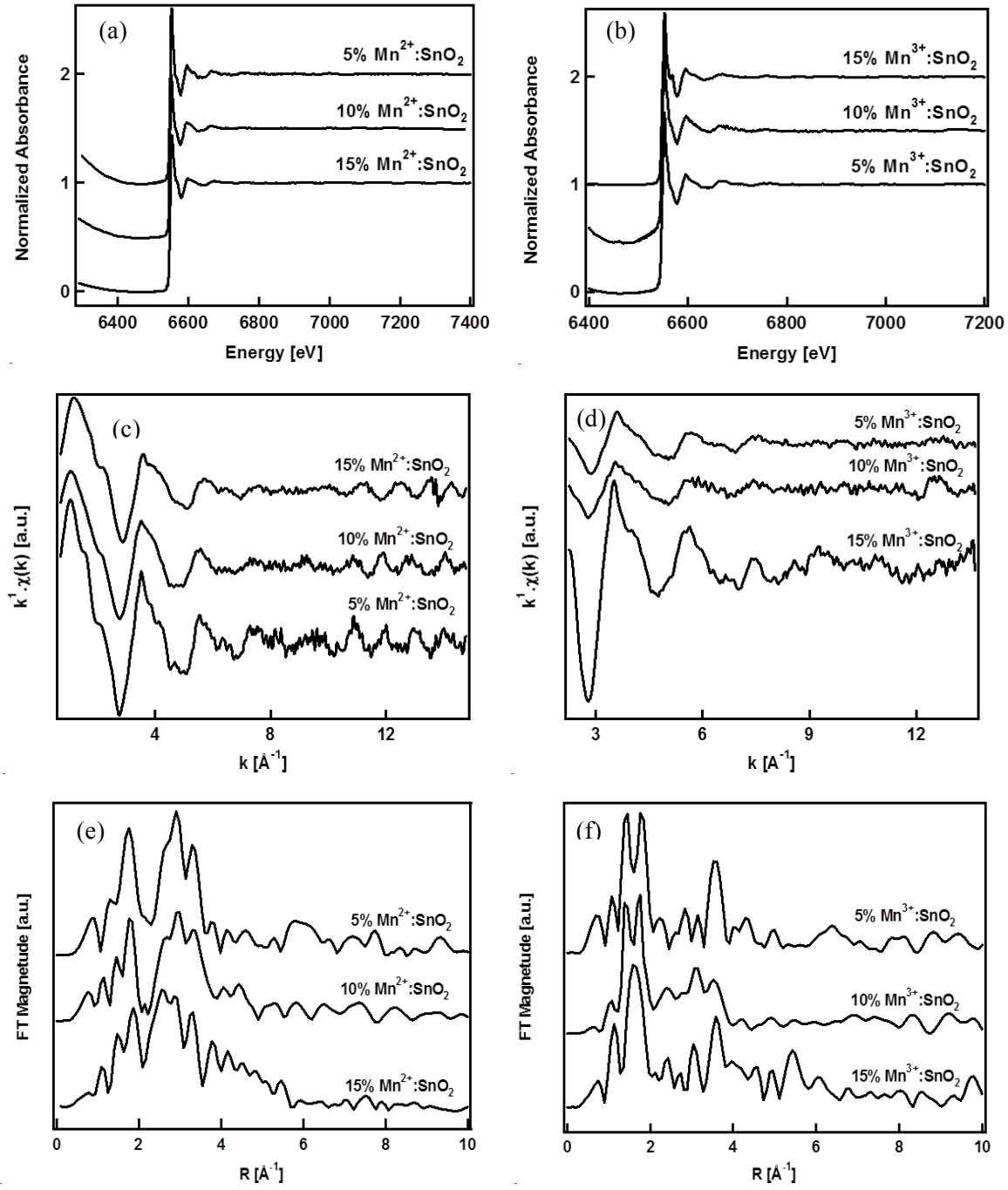

Figure 3-12: (a) and (b) Full spectral range of Mn K-edge absorption spectra for Mn^{2+}:SnO_2 and Mn^{3+}:SnO_2, (c) and (d) k-weighted Mn K-edge EXAFS spectra for Mn^{2+}:SnO_2 and Mn^{3+}:SnO_2, (e) and (f) Pseudo-radial distribution function obtained by Fourier transformation of Mn^{2+}:SnO_2 and Mn^{3+}:SnO_2 EXAFS spectra.

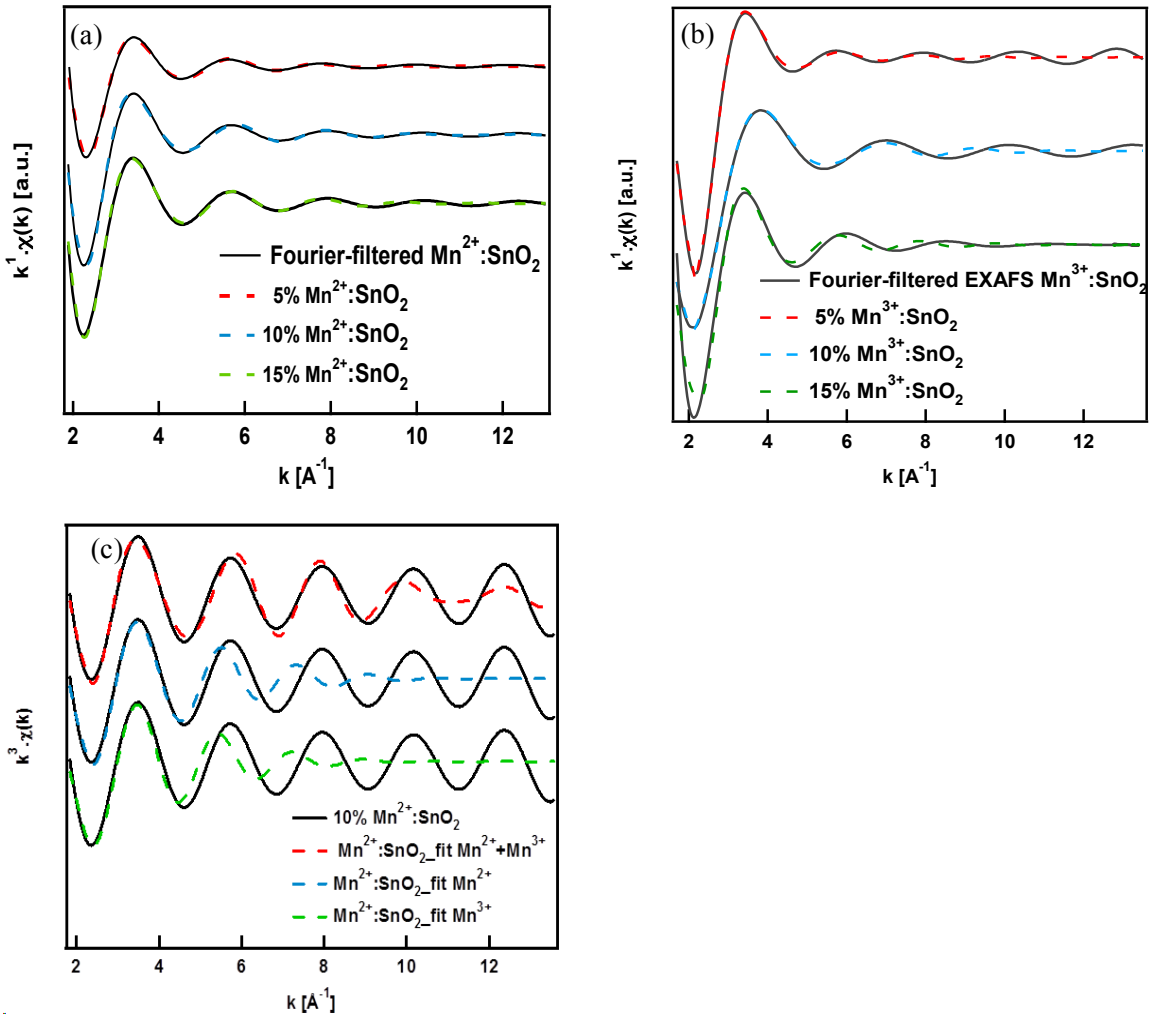

Figure 3-13: (a) and (b) Fourier-filtered EXAFS spectra for the first shell (Mn-O) of Mn^{2+}:SnO_2 and Mn^{3+}:SnO_2 nanocrystal, respectively, (c) comparison between the Fourier-filtered oscillations of the first shell (Mn-O) for fitting with characteristic parameters of Mn^{2+}, Mn^{3+} and combination of the two. The spectra are weighted by k^3 to compensate with the decrease in EXAFS oscillations amplitude at higher k values.

Table 3-4: Results from the EXAFS analysis of Mn^{2+}: SnO_2 and Mn^{3+}: SnO_2 for the first Mn-O shell.

Sample	Dopant Concentration	N	Bond Distance (Mn^{2+}-O) (Å)	Bond Distance (Mn^{3+}-O) (Å)	σ^2 (Mn^{2+}) ($Å^2$)	σ^2 (Mn^{3+}) ($Å^2$)	ρ (%)
Mn^{2+}:SnO_2	5%	6	2.12	1.94	0.007	0.007	0.74
	10%	6	2.08	2.01	0.019	0.019	0.55
	15%	6	2.02	1.95	0.012	0.019	0.71
Mn^{3+}:SnO_2	5%	6	2.08	2.02	0.024	0.044	2.37
	10%	6	2.09	1.98	0.090	0.039	2.67
	15%	6	2.08	2.00	0.045	0.045	6.00

N: Number of nearest neighbors, σ: Debye-Waller factor, ρ: Weighted residual factor

Chapter 4
Structural Analysis of Mn-Doped In_2O_3

Structural analysis of Mn^{2+}:In_2O_3 and Mn^{3+}:In_2O_3 has been studied in this chapter. With the same strategy of the chapter 3, we first review the morphological and structural parameter of Mn-doped In_2O_3 (that we used for the XAS analysis) using TEM and XRD analysis. And then we focus on the electronic structure of the synthesized nanoparticles through X-ray absorption spectroscopy, including EXAFS and XANES.

4.1 Review of Mn:In_2O_3 Properties

Figure 4-1 represents TEM images and a size distribution histogram for the pure and Mn-doped In_2O_3. The nanocrystals are synthesized at 250 °C for 1h. The concentration of dopant ($Mn(acac)_3$) with respect to $In(acac)_3$ varies from 0 to 15%. Starting from pure In_2O_3, the size distribution histogram confirms that the size of prepared nanoparticles is ca. 8.5 nm with relatively narrow distribution. Introducing manganese as dopant affectedly changes the distribution function: small nanoparticles with the size of 4 nm and large nanoparticles with average size of ca. 8.5 nm. Increasing the Mn^{3+} concentration to 10%, fraction of small nanoparticles increases, while larger nanoparticles decrease in number and they disappear at 15% at which the size of nanoparticles is ca. 4.5 nm.

As the size of nanoparticles decreases with increasing dopant concentration, changes in the crystal structure of the prepared nanoparticles have also been observed. Figure 4-2 represents the high resolution (HRTEM) images for 10% Mn^{3+}: In_2O_3 for small and large nanoparticles. The d-spacing of ca. 2.74 Å calculated for small NCs corresponds to {110} lattice plane of rhombohedral indium oxide (rh-In_2O_3), and the d-spacing of 2.91 Å that was observed in larger NCs can be attributed to {222} lattice plane of bixbyite indium oxide (bcc-In_2O_3).

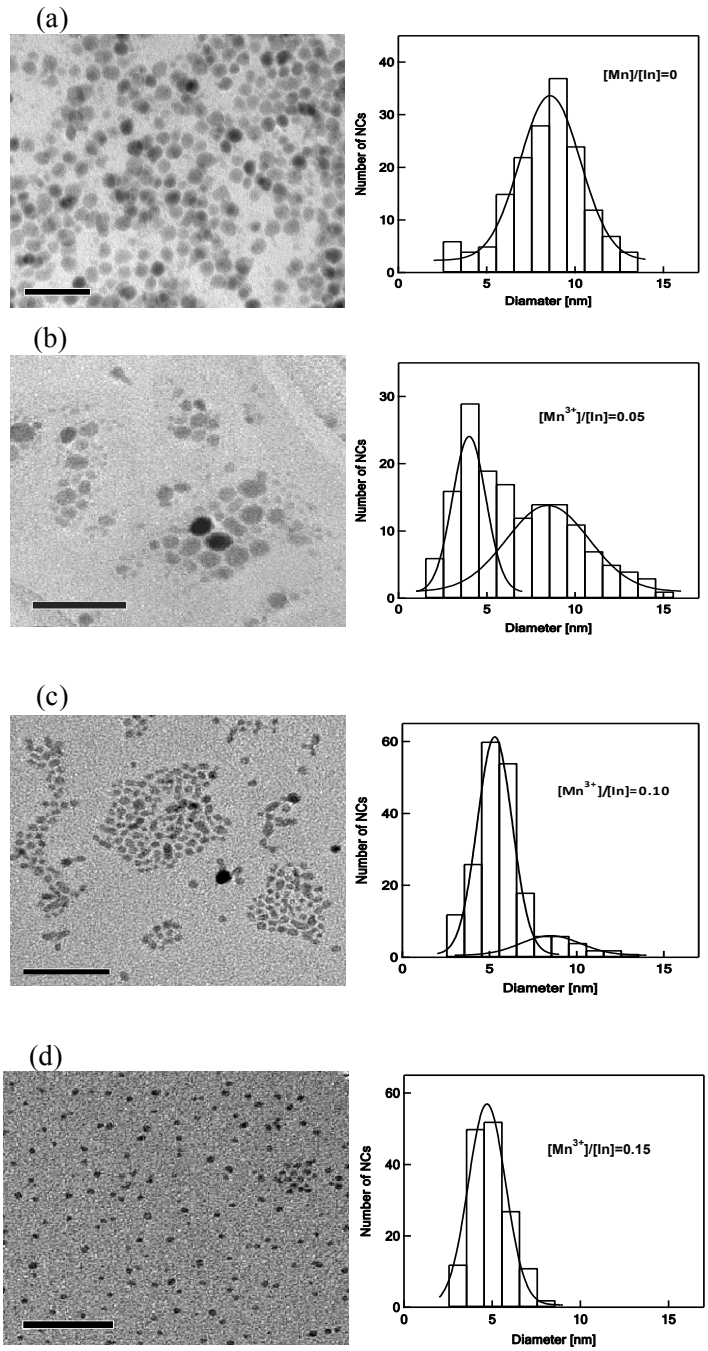

Figure 4-1: TEM images (left) and size distribution histogram (right) of Mn-doped In_2O_3 nanoparticles with varying $\frac{[Mn]}{[In]}$ ratio (a) 0, (b) 0.05, (c) 1 and finally (d) 1.5 (Scale bars in TEM micrographs are 50 nm).[58]

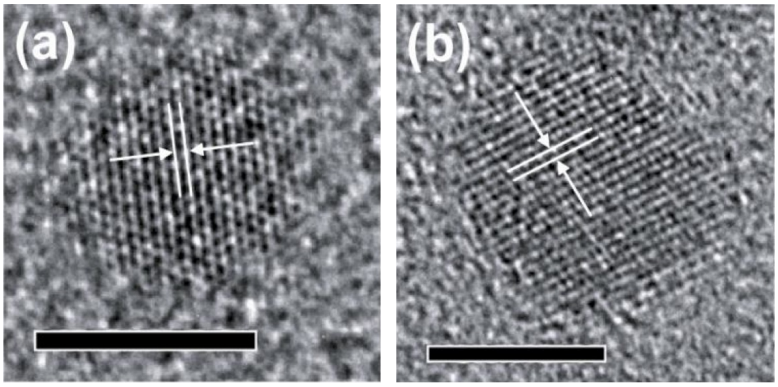

Figure 4-2: HRTEM images of 10% Mn^{3+}: In_2O_3 NCs confirming the phase transformation by decreasing the size of nanoparticles. Lines and arrows show the d-spacing. (a) The average d-spacing for small particles is 2.74 Å, which corresponds to the {110} lattice plane in rh-In_2O_3 and (b) the average d-spacing for large nanoparticles is 2.91 Å, which represents {222} lattice plane in bcc-In_2O_3.[58] The scale bars are 5 nm.

The same trend is also observed for In_2O_3 NCs doped with Mn^{2+}(Figure 4-3). Introducing 5% of dopant leads to a decrease in the size of indium oxide nanoparticles from ca. 8.5 nm for pure In_2O_3 to 7.4 nm for 5% Mn^{2+}: In_2O_3 showing the narrower size distribution. Further increase in concentration of Mn^{2+} dopant is associated with the appearance of bimodal size distribution: 65% of nanoparticles representing an average size of ca. 6.1 nm with a narrow size distribution, while the average size of the rest of Mn^{2+}: In_2O_3 NCs is ca. 13.8 nm with a broad distribution. Average sizes for 15% and 20% Mn^{2+}-doped In_2O_3 are 4.4 and 4.2 nm, respectively.

HRTEM micrographs reveal phase transition upon increasing Mn^{2+} concentration from bixbyite structure with d-spacing 2.91 Å corresponding to {222} lattice plane to rhombohedral structure with inter-planar spacing of 2.74 Å consistent with {110} planes (Figure 4-4).

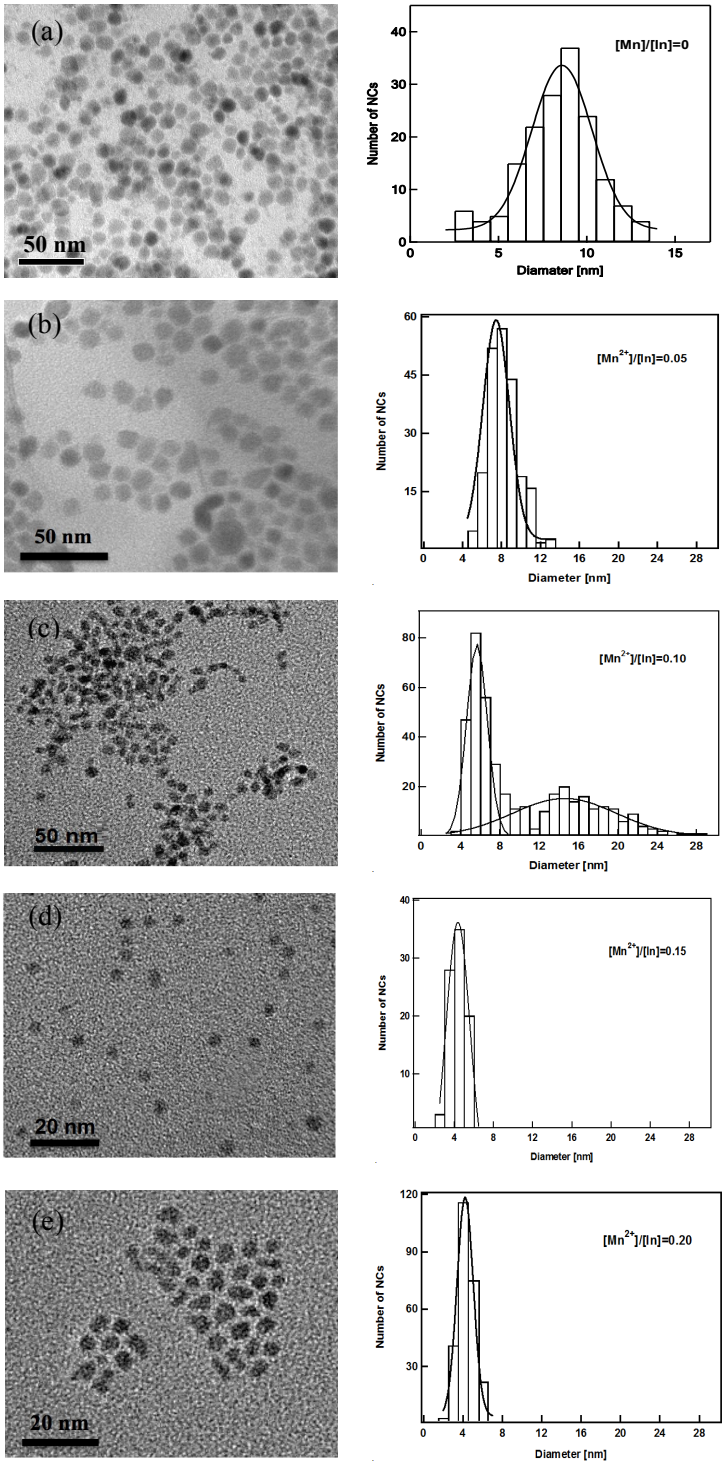

Figure 4-3: Overview of TEM images and size distribution histograms with Mn^{2+} vs. In precursor molar ratios ($\frac{[Mn^{2+}]}{[In]}$) of (a) 0, (b) 0.05, (c) 0.10, (d) 0.15 and (e) 0.20.

Observed phase transformation is also confirmed by XRD analysis (Figure 4-5). Pure In_2O_3 NCs show a bixbyite structure. Increasing the dopant concentration, the formation of rhombohedral structure is evident in XRD patterns. Rhombohedral structure, which is associated with a decrease in the size of NCs results in the broadening of XRD peaks at higher dopant concentrations.

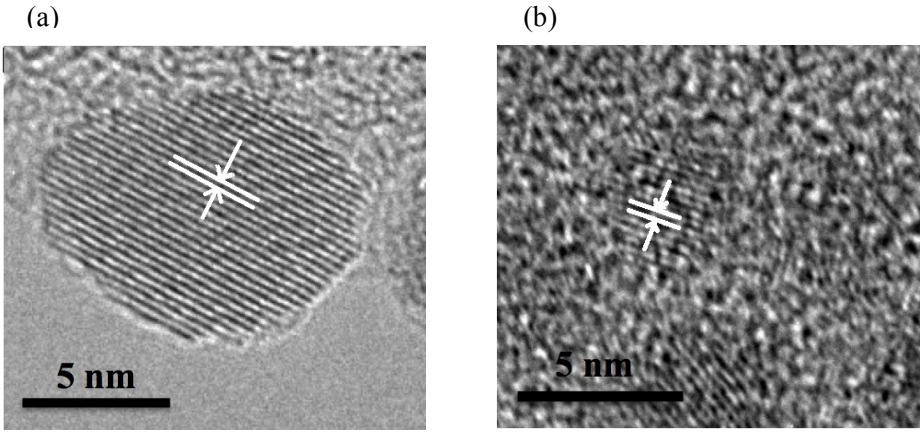

Figure 4-4: (a) HRTEM image for 5% Mn^{2+}: In_2O_3 NCs. Nanoparticles have average size of ca. 7.4 nm and the d-spacing is 2.91 Å corresponding to {222} plane in bixbyite structure and (b) HRTEM image for 20% Mn^{2+}: In_2O_3 nanoparticles with d-spacing of 2.91 Å representing {111} lattice plane in rhombohedral structure.

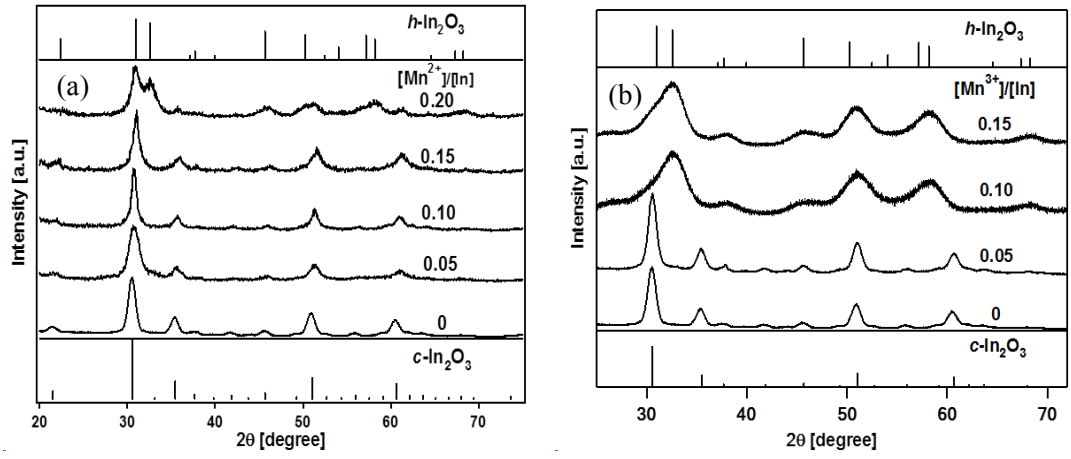

Figure 4-5: XRD patterns of (a) Mn^{2+}: In_2O_3 and (b) Mn^{3+}: In_2O_3 with different Mn vs. In molar ratios. The black lines are the patterns of bulk bcc-In_2O_3 (bottom, JCPDS 06-0416) and rh-In_2O_3 (top, JCPDS 21-0406).

Farvid *et al.* has shown that introducing dopants into the In_2O_3 host lattice is not necessary to induce phase transformation from cubic to rhombohedral structure. Instead, bounded dopant ions to the surface of In_2O_3 NCs inhibit the growth mechanism and lead to the stabilization of metastable phases. This is a general phenomenon for polymorphic materials where different crystal structures have relatively close potential energy minima.[58]

4.2 Manganese K-Edge Measurements

Figure 4-6 illustrates Mn K-edge XANES spectra acquired in fluorescence mode for ensembles of indium oxide nanocrystals doped with varying concentrations of Mn^{2+} and Mn^{3+} as dopants. Mn K-edge XANES spectra of standard manganese oxides with different oxidation states, 2+ (MnO), 2.67+ (Mn_3O_4), 3+ (Mn_2O_3) and 4+ (MnO_2), are presented as a guide to the valence state of manganese ions. The first feature observed in pre-edge region is the peak at 6540 eV and is accompanied by a strong white line above the absorption edge, which is characteristic for substitution of Mn ion in In^{3+}site in In_2O_3 NCs.[59] The pre-edge absorption peak results from dipole-forbidden 1s-3d transition and is strongly influenced by degree of asymmetry around the absorbent atom. So, the low intensity of pre-edge absorption edge exhibits slightly distorted structure from octahedral structure.

Compared to standard manganese oxides, the Mn K-edge of the Mn:In_2O_3 NCs changed shape and shifted to higher energy values as the irradiation proceeded. The changes in the shape of the spectral profile compared to standard manganese oxides confirm the presence of Mn as dopants in In_2O_3 host lattice, rather than formation of manganese oxide clusters. For all Mn^{2+}:In_2O_3 and Mn^{2+}:In_2O_3 samples, the peak position shifts from MnO absorption edge towards Mn_2O_3 edge verifying that manganese oxidation state lies between 2+ and 2.67+. Figure 4-7 represents the absorption edge energy vs. oxidation state for Mn^{2+}:In_2O_3 and Mn^{2+}:In_2O_3 NCs, respectively. Absorption edge energies of reference compounds have also been presented to use for energy calibration. Summary of results analyzed from Mn K-edge XANES spectra of the synthesized samples are presented in Table 4-1. Table 4-1 demonstrates that increasing Mn^{2+} concentration from 5% to 10% results in increasing manganese oxidation state from 2.53+ to 2.58, and then it drops to 2.45+ as the dopant concentration reaches 20%. Presence of 40-53% Mn^{3+}, which is also confirmed by UV-Vis and PPMS data, is the result of oxidation process that converts a fraction of Mn^{2+} starting precursors to Mn^{3+}. The same results are also observed for Mn^{3+}:In_2O_3 synthesized nanocrystals. Increasing Mn^{3+} concentration from 2% to 5% leads to the formation of 36% and 31% of Mn^{2+} species, respectively. Unexpectedly,

an increase in fraction of Mn^{2+} species up to 68% is experienced by introducing 10% Mn^{3+} as dopant. Final fraction of Mn^{2+} is ca. 56%, which is observed in 20% Mn^{3+}:In_2O_3 nanocrystals. Therefore, the final Mn-doped In_2O_3 NCs contain both Mn^{2+} and Mn^{3+} independently of the type of starting precursor.

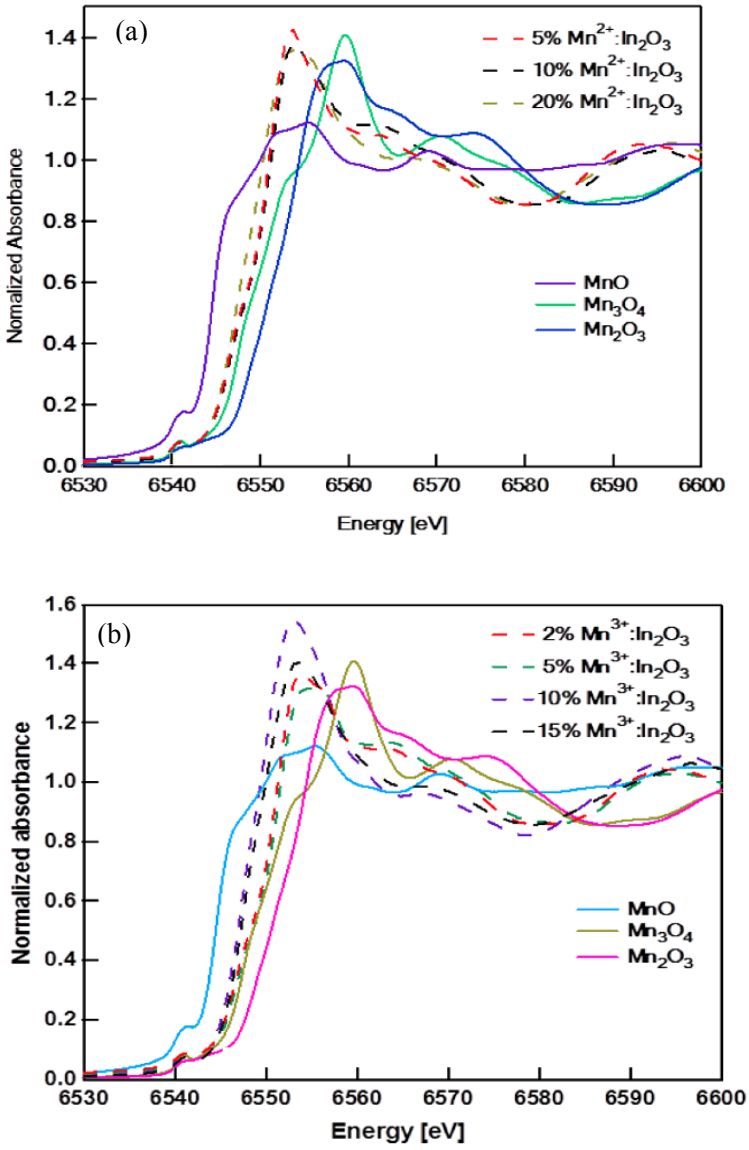

Figure 4-6: XANES spectra for (a) Mn^{2+}-doped In_2O_3 NCs and (b) Mn^{3+}-doped In_2O_3 NCs with different dopant concentrations in comparison with manganese oxides with different oxidation states.

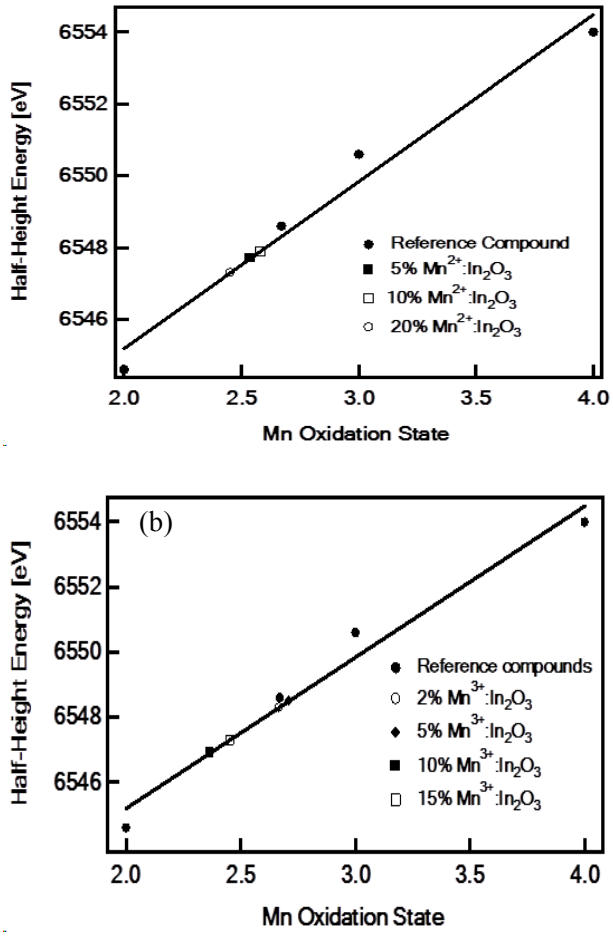

Figure 4-7: Half-height energy obtained from analysis of Mn K-edge XANES spectra vs. manganese oxidation state for (a) Mn^{2+}-doped In_2O_3 and (b) Mn^{3+}-doped In_2O_3 NCs with varying $\frac{[Mn]}{[In]}$ molar ratios. Manganese oxides used as reference compounds to calibrate the energy.

Table 4-1: Summary of data from Mn K-edge analysis of Mn^{2+}:In_2O_3 and Mn^{3+}:In_2O_3 NCs with varying doping concentration.

Sample	Dopant Concentration	Energy Edge (eV)	Oxidation State	$\frac{Mn^{2+}}{Mn^{2+}+Mn^{3+}}$ (%)
Mn^{2+}:In_2O_3	5%	6546.04	2.53	43.1%
	10%	6545.67	2.58	39.4%
	20%	6546.01	2.45	53.4%
Mn^{3+}:In_2O_3	2%	6548.3	2.67	36.1%
	5%	6548.5	2.71	30.6%
	10%	6546.9	2.36	68.1%
	15%	6547.3	2.45	56.1%

To study the local structure of the manganese dopants, EXAFS are acquired at Mn K-edge. Figure 4-8 displays the k-weighted Fourier-filtered EXAFS oscillations for Mn^{2+}-doped In_2O_3 and Mn^{3+}-doped In_2O_3 nanocrystals with varying $\frac{[Mn]}{[In]}$ ratios. The structural parameters obtained from the fitting of Fourier-filtered EXAFS spectra with linear combination of Mn-O distances characteristic for Mn^{2+}

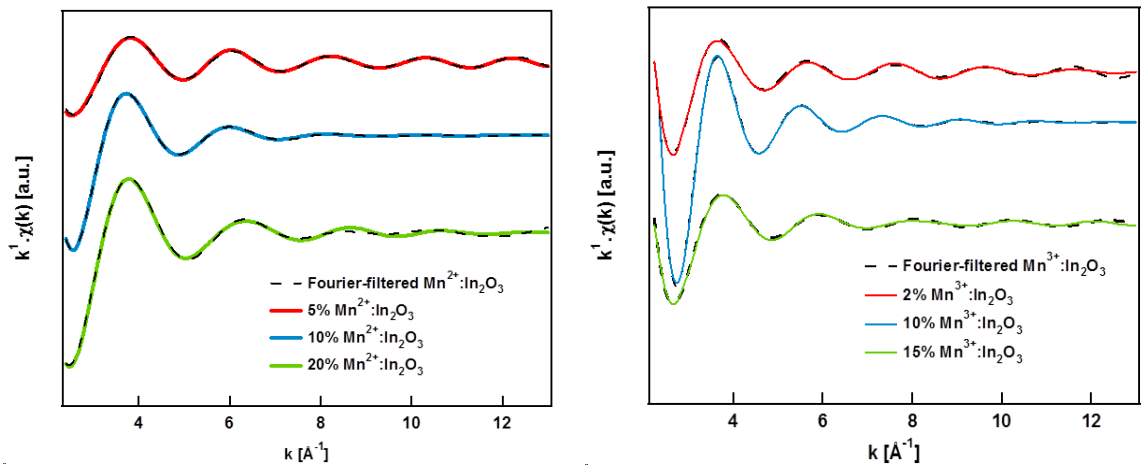

Figure 4-8: Fourier-filtered EXAFS oscillations for (a) Mn^{2+}: In_2O_3 and (b) Mn^{3+}: In_2O_3 NCs with different dopant concentration: experimental data (dashed line) and fitting results (solid line).

Table 4-2: Results from the EXAFS analysis of Mn^{2+}: In_2O_3 and Mn^{3+}: In_2O_3 for the first Mn-O shell

Sample	Dopant Concentration	N	Bond Distance (Mn^{2+}-O) (Å)	Bond Distance (Mn^{3+}-O) (Å)	σ^2 (Mn^{2+}) ($Å^2$)	σ^2 (Mn^{3+}) ($Å^2$)	ρ (%)
Mn^{2+}:In_2O_3	5%	6	2.11	1.94	0.005	0.002	0.34
	10%	6	2.11	1.96	0.034	0.018	0.54
	20%	6	2.17	1.89	0.020	0.009	0.46
Mn^{3+}:In_2O_3	2%	6	1.93	1.73	0.011	0.034	0.92
	10%	6	2.19	1.87	0.008	0.021	0.10
	15%	6	2.17	2.07	0.005	0.005	0.49

(in MnO) and Mn^{3+} (in Mn_2O_3) that has been used as initial parameters. Similar to Mn:SnO_2 NCs, a linear combination of both Mn^{2+} and Mn^{3+}parameters is needed to gain better fitting results. Table 4-2 demonstrates the fitting results obtained from EXAFS analysis of Mn^{2+}: In_2O_3 and Mn^{3+}: In_2O_3 NCs. Results summarized in Table 4-2 are in a good correlation with crystallographic data. According to the literature, the average In-O bond distance in cubic bixbyite and rhombohedral structure is 2.17-2.18 Å.[28, 60, 61] Considering close ionic radii of Mn^{2+} and In^{3+}, 0.83 Å and 0.80 Å, respectively, we expect that Mn^{2+}-O and In-O should have very similar bond distances. XANES analysis reveals that 20% Mn^{2+}: In_2O_3, 10% and 15% Mn^{3+}: In_2O_3 NCs include the highest fraction of Mn^{2+}, which according to Table 4-2 show closer Mn^{2+}-O bond distances to In-O bond length. In other samples, Mn^{3+}, with ionic radius of 0.65 Å, is the dominant species and leading to the decrease in Mn^{2+}-O and Mn^{3+}-O bond distances that is associated with the shrinking of the host lattice, mainly observed in fitting results for 2% Mn^{3+}: In_2O_3 NCs.

Chapter 5

Optical and Magnetic Properties of Mn-Doped SnO_2 and In_2O_3 NCs

In this chapter we study the spectroscopic and magnetic properties of Mn-doped SnO_2 and In_2O_3 NCs in colloidal form and their film form. Magnetic properties of the synthesized nanocrystals have been studied using magnetic susceptibility and MCD analysis. Ferromagnetic ordering observed in nanocrystalline films prepared from paramagnetic free-standing NCs which resulted from the extended NC interfacial defects in such films.

5.1 Electronic Absorption And Magnetic Circular Dichroism Spectroscopies

Free Mn^{2+} ion has a $3d^5$ electronic configuration and can be considered as a model system with half-filled *3d* shell. The high spin ground state (all five electrons being parallel) is the singlet ^{6}S and the next excited state are ^4G, ^4P, ^4D etc. (Figure 5-1). All transitions from ground state to excited doublet levels are forbidden; transitions to quartet levels are also forbidden in free Mn^{2+} ion. Ground state sextet, ^6S, cannot be split in any crystal field, which means all ground state absorption transitions in the high spin d^5 are spin forbidden and are silent in spectroscopic analysis.[62]

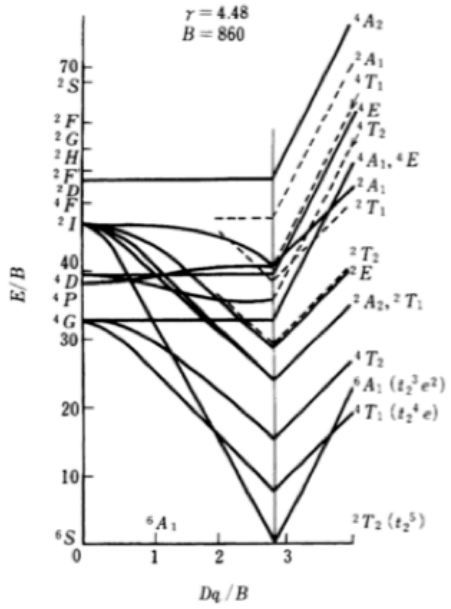

Figure 5-1: Energy level diagram for d^5 configuration.[63]

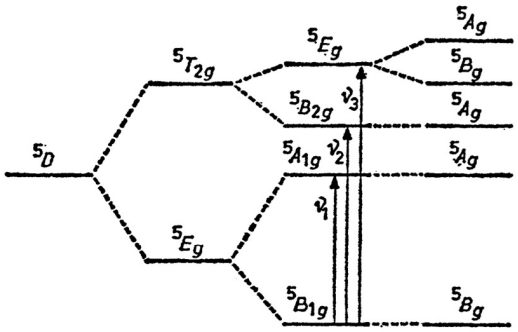

Figure 5-2: Energy level diagram for a d^4 configuration in a tetragonal and rhombic (C_{2h}) symmetry.[64]

Energy level diagram for Mn^{3+} ion in ideal and distorted octahedral is presented in Figure 5-2. High spin Mn^{3+} (d^4) belongs to ground state ^5D. In the ideal octahedral (O_h) symmetry, this energy level splits into $^5T_{2g}$ and ^5E_g terms, giving a characteristic spin allowed transition $^5E_g \rightarrow {}^5T_{2g}$, which appears around 20000 cm^{-1}. Mn^{3+} ion is subjected to Jahn-Teller distortion that decreases the symmetry of the coordination site from octahedral (O_h) to tetragonal (D_{4h}) and in lower symmetry to rhombic (C_{2v}). In tetragonal symmetry $^5T_{2g}$ splits into ^5E_g and $^5B_{2g}$ levels and ^5E_g orbital splits to $^5A_{1g}$ and $^5B_{1g}$ leading to appearance of 3 absorption bands: $^5B_{1g} \rightarrow {}^5A_{1g}$, $^5B_{1g} \rightarrow {}^5B_{2g}$ and finally $^5B_{1g} \rightarrow {}^5E_g$. In rhombohedral symmetry ^5E_g splits to ^5A_g and ^5B_g giving rise to 4 absorption bands.[64, 65]

Optical absorption spectra for 10% Mn^{2+}:SnO_2 nanocrystals are displayed in Figure 5-3 (a). According to aforementioned discussion Mn^{2+} ion, substituting tin site at the center of octahedral oxygen cage, is spectroscopically quiet. The peak observed at 530 nm corresponds to the energy of 19000 cm^{-1}. This peak is characteristic feature of Mn^{3+} in octahedral symmetry that can be assigned to spin-allowed $^5E_g \rightarrow {}^5T_{2g}$ transition in octahedral environment. So, the presence of a $^5E_g \rightarrow {}^5T_{2g}$ transition in Mn^{2+}-doped SnO_2 NCs confirms formation of Mn^{3+} ion during the synthesise process, agreeing with Mn K-edge XANES analysis. The band gap transition of host SnO_2 nanocrystals is observed as a shoulder at ~335 nm and is estimated to be 3.6 eV. This band gap energy that lies at higher energies relative to bulk tin oxide is consistent with the structural information of SnO_2 nanocrystals discussed in section 1.1.1.

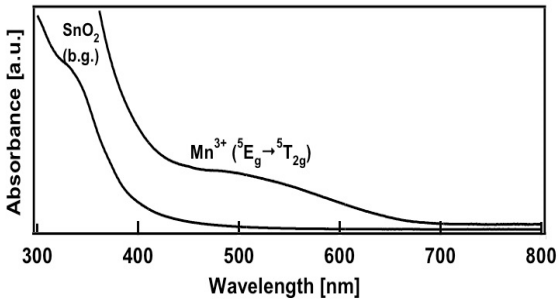

Figure 5-3: Optical absorption spectrum of 10% Mn^{2+}-doped SnO_2 NCs showing characteristic feature of Mn^{3+} in octahedral environment and band gap transition.

Optical absorption spectra for Mn-doped In_2O_3 NCs follow the same rules. Figure 5-4 (a) and Figure 5-5 (a) show optical absorption spectra (top) and corresponding 4.5 K MCD spectra (bottom) collected in varying magnetic field ($B = 1 - 7$ T) for 10% $Mn^{2+}:In_2O_3$ and 20% $Mn^{2+}:In_2O_3$ nanocrystals with different crystal structures, bixbyite and rhombohedral, respectively. Low energy transition for the bixbyite structure occurs at 546 nm (~18300 cm^{-1}) and for the rhombohedral structure happens at 520 nm (~19000 cm^{-1}). This transition can be assigned to spin-allowed $^5E_g \rightarrow {}^5T_{2g}$ transition in octahedral environment.[66, 67] Figure 5-4 (b) demonstrates the MCD intensity at 546 and 384 nm plotted as a function of applied magnetic field ($\frac{\beta H}{2kT}$) at constant temperature ($T = 4.5$ K). Similarly, Figure 5-5 (b) represents MCD intensity at peak position vs. magnetic field. All features show saturation magnetization, confirming that magnetization comes from isolated paramagnetic Mn^{3+} (note that Mn^{2+} is spectroscopically silent). Magnetization of paramagnetic transition metal ion is often described by Brillouin function:

$$M_s = \frac{1}{2} N g \mu_B \left[(2S+1)\coth\left((2S+1)\left(\frac{g\mu_B H}{2k_B T}\right)\right) - \coth\left(\frac{g\mu_B H}{2k_B T}\right)\right] \qquad \text{Equation 5-1}$$

Where M_s is the saturation magnetization, g is the Lande-factor, H is the applied magnetic field, S is the spin quantum number, μ_B is the Bohr magneton, k_B is the Boltzmann constant and T is the absolute temperature. According to the literature, Lande-factor for Mn ion in rhombohedral and cubic oxides is $g \approx 1.99 - 2.00$.[68, 69] The intensity saturates at high magnetic field and low temperatures. The best ftting results come from considering only spin state of Mn^{3+} ion (S=2) substituting In^{3+} in In_2O_3 host lattice, and the linear combination ($N_{Mn^{2+}}M_{Mn^{2+}} + N_{Mn^{3+}}M_{Mn^{3+}}$) leads to $N_{Mn^{2+}} \approx 0$.

Fitting with spin only Brillouin function is the result of absence of orbital angular momentum in the ^5E_g ground state of Mn^{3+}.

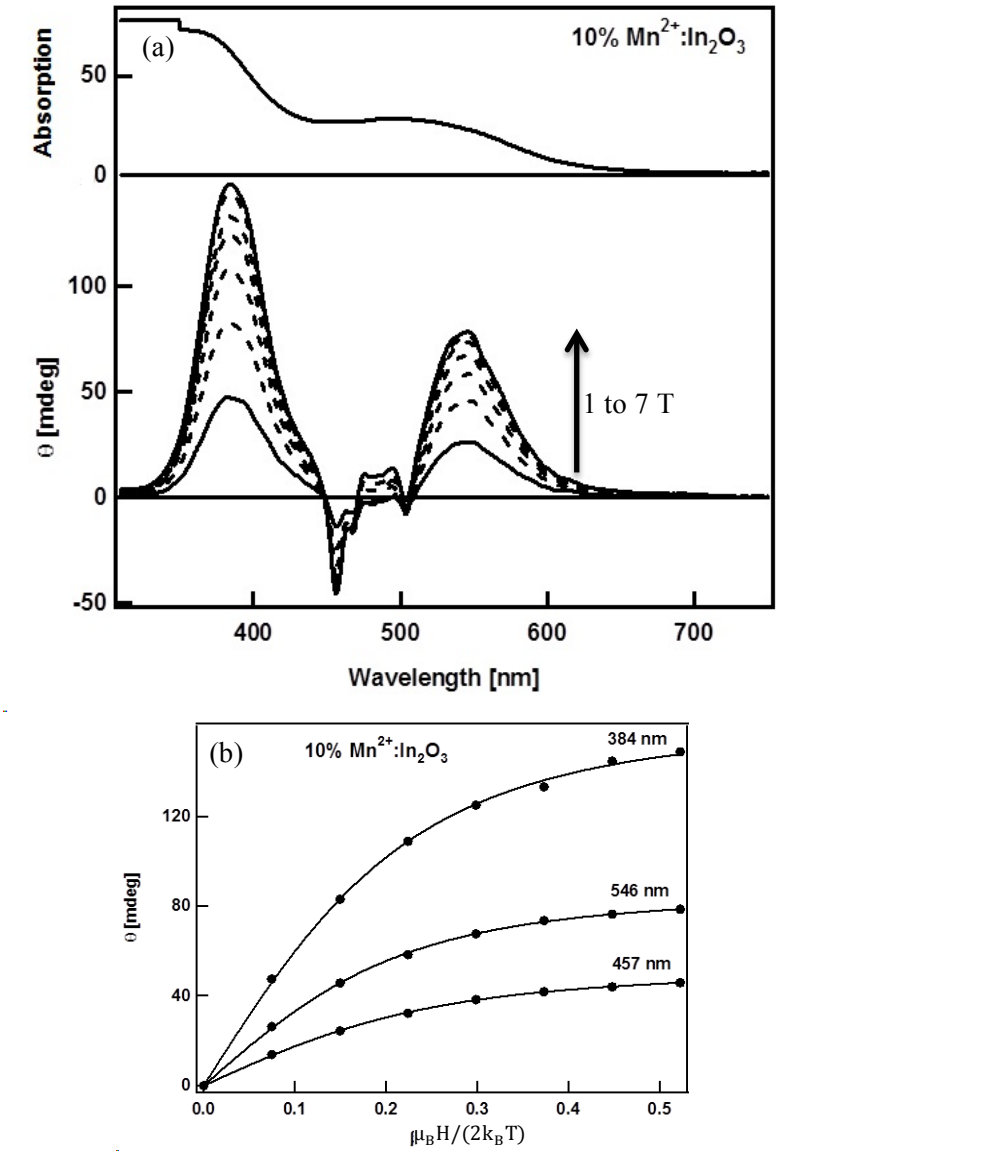

Figure 5-4: (a) 4.5 K electronic absorption spectrum of bixbyite 10% Mn^{2+}: In_2O_3 nanocrystalline film at room temperature (top) and MCD spectra of the same sample at 4.5 K, collected at varying magnetic field from 1-7T (bottom). (b) MCD intensity at 546, 384 and 457 nm vs. magnetic field. The black lines are fits to the Brillouin function.

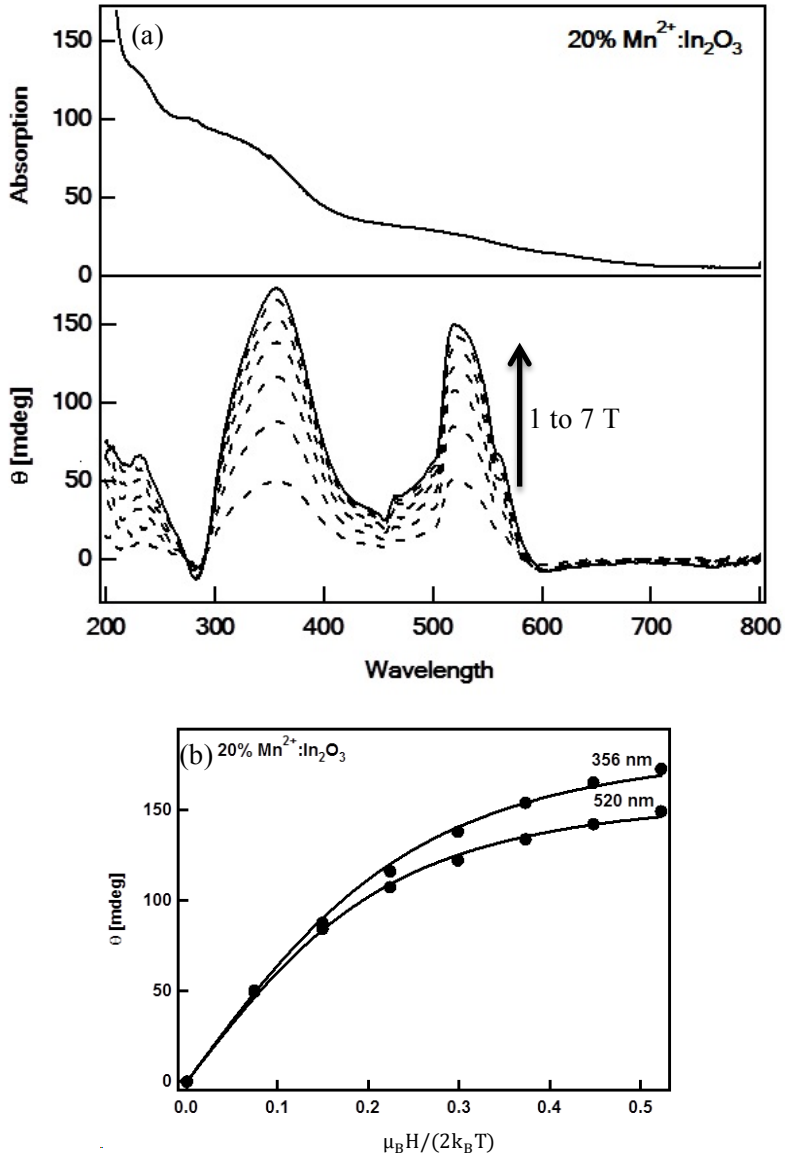

Figure 5-5: (a) 4.5 K electronic absorption spectrum of bixbyite 20% Mn^{2+}: In_2O_3 NCs (top) and MCD spectra of the same sample at 4.5 K, collected at varying magnetic field from 1-7T (bottom). (b) MCD intensity at 520 and 356 nm vs. magnetic field. The black lines are fits to the Brillouin function.

5.2 Magnetism

Magnetization properties for 5% Mn^{2+}: SnO_2 NCs collected at 5 K and 300 K are shown in Figure 5-6(a). It is well established that nanocrystalline films fabricated from free-standing NCs demonstrate saturation magnetization and small hysteresis loops representing ferromagnetic properties.[40, 70, 71] Decrease in temprature results in an increase in saturation magnetization and hysteresis coercivity. Figure 5-6 (b) shows saturation magnetization vs. temprature for differenet magnetic field strengths. The ferromagnetic phase transformation has not been observed up to 300 K, which indicates that the Curie temprature, T_c, should be above room temprature.

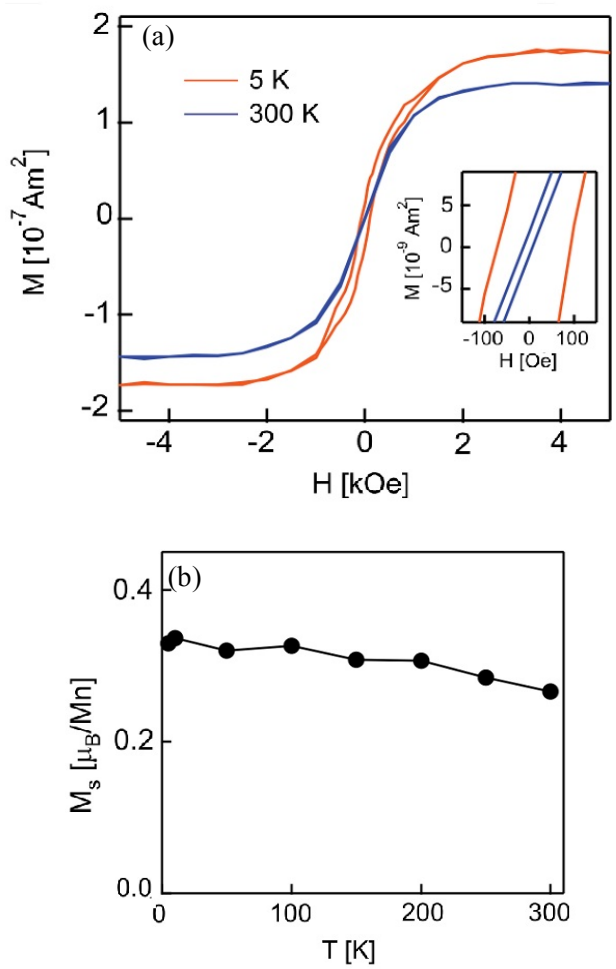

Figure 5-6: (a) Magnetization hysteresis loop for 5% Mn^{2+}: SnO_2 nanocrystalline film collected at 5 K (red) and 300 K (black). The inset shows magnified hysteresis loops around H = 0. Both loops are corrected for diamagnetic contribution. (b) Temperature dependence of saturation magnetization for Mn-doped SnO_2 nanocrystalline films.[45]

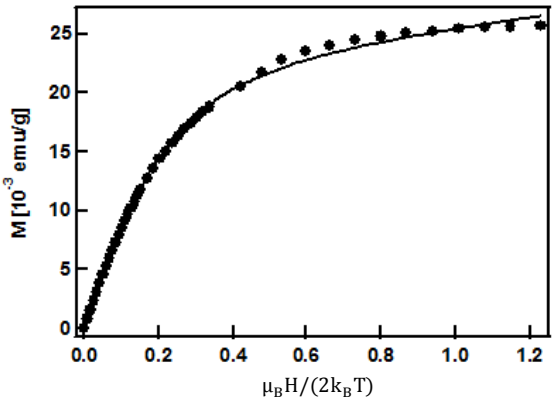

Figure 5-7: 2 K saturation magnetization of free standing 15% Mn^{2+}: SnO_2 NCs (black circles). The experimental data fitted with Brillouin function assuming equal contribution of Mn^{2+} and Mn^{3+}.

Free standing Mn-doped SnO_2 NCs exhibit paramagnetic behavior. Figure 5-7 shows saturation magnetization for 15% Mn^{2+}: SnO_2 NCs collected at 2 K fitted with Brillouin function. Neither of Mn^{2+} nor Mn^{3+} leads to good fitting results with the experimental data, while a linear combination of both species, $M_s = xM_s(Mn^{2+}) + yM_s(Mn^{3+})$ with criteria $(x + y = 1)$ matches very well with the recorded data for $x = y \approx 0.5$. Equal contribution of Mn^{2+} and Mn^{3+} in Brillouin function is in agreement with Mn K-edge XANES data discussed in section 3.2.

10% Mn^{2+}: In_2O_3 and 10% Mn^{3+}: In_2O_3 NCs in powder form exhibit paramagnetic behavior. Corresponding saturation magnetization is represented in Figure 5-8 (a) and (b) , respectively. The criteria applied on the brillouin function is the same as Mn-doped SnO_2 nanocrystals. For 10% Mn^{2+}-doped In_2O_3, the contribution of Mn^{2+} and Mn^{3+} is in excellent agreement with X-ray absorption spectroscopy data. The calculations reveal that after subtraction of diamagnetic behavior, it is ca. 60% for Mn species is Mn^{3+} and ca. 40% is Mn^{2+}. In the case of 10% Mn^{3+}: In_2O_3 NCs, 30% Mn^{3+} and 70% Mn^{2+} contribute to the recorded saturation magnetization, which is in excellent match with XANES data.

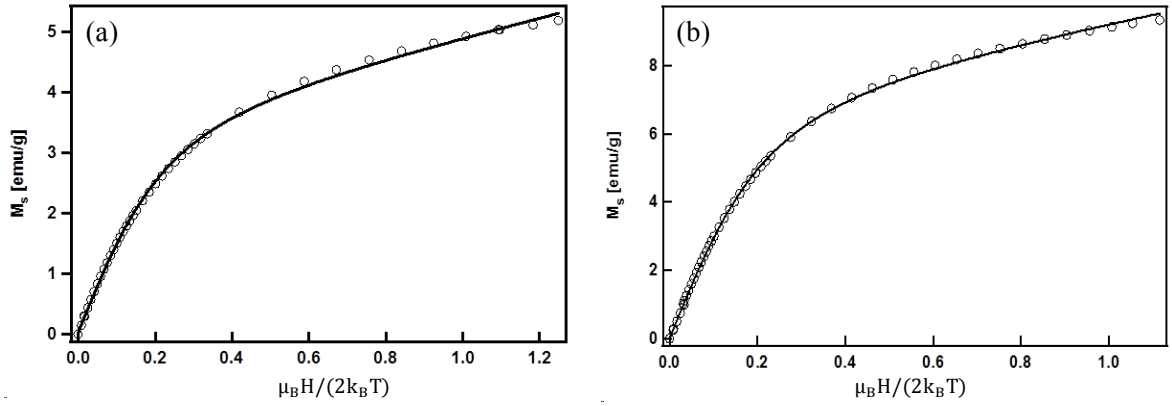

Figure 5-8: Saturation magnetization for (a) 10% $Mn^{2+}:In_2O_3$ and (b) 10% $Mn^{3+}:In_2O_3$ paramagnetic nanocrystals. Open circles are the experimental data recorded at 2 K and the black lines are the results for fitting with Brillouin function.

It should be also noted that ferromagnetism is absent in pure In_2O_3 NCs at room temperature. Abraham *et al.* has shown that the mesurable ferromagnetic signal observed in nonmagnetic hafnium oxide (HfO_2) nanocrystalline thin film is the result of contamination from handelling with stainless-steel tweezers. This report claims that magnetic properties of the contamination is smilar with ferromagnetic behavior of hafnium oxide.[72] In our magnetic measurements, the handeling of all undoped and doped samples is done identically and in carfully controlled nonmagnetic environment.

The main conclusions derived after studying magnetic behavior in Mn-doped SnO_2 and Mn-doped In_2O_3 can be summarized as following: (1) as-synthesized free-standing doped nanoparticles exhibit paramagnetic behavior. (2) paramagnetism originates from isolated Mn^{2+} and Mn^{3+} ions that substitute Sn^{4+} and In^{3+} sites in SnO_2 and In_2O_3 host lattice, respectively. (3) The presence of different oxidation states determines the magnetization behavior of the samples which is in agreement with X-ray absorption spectroscopy (XAS) analysis. (4) interfacial structural defects during preparation of nanocrystalline thin film play an mportant role in long range-ordering of substitutionally incorporated tarnsition metal dopant ions in the nanocrystal network.

The origin of ferromagnetism in nanocrystalline DMSO is of great fundamental importance and it is still under debate. Recent experimental and theoretical explorations demonstrate that the charge carriers are responsible for long-range ferromagnetic interactions, which means that changes in carriers concentration will affect the ferromagnetic prperties. Tin oxide and indium oxide are n-type semiconductors. Based on bound magnetic polaron proposed by Coey, donor impurity (oxygen

vacancy) band hybrideze with dopant d-state at the fermi level, mediating long-range magnetic interactions.[34] $Mn^{2+}(3d^5)$ has two electrons in e_g energy level in an octahedral environment. Since the e_g orbital is directed towards O 2p orbital, the hybridization of Mn 3d orbital with the donor impurity band at the fermi level leading to formation and stabilization of high-T_c ferromagnetism. Since the extent of 3d orbitals increases with decreasing number of 3d electrons, increasing Mn^{3+} concentration at the expense of Mn^{2+} concentration leads to the weakening of the hybridization of Mn^{3+} 3d and donor impurity band and results in diminished magnetization.[73]

Philip *et al.* [74] have shown that increasing in defect concentration can tune the magnetic interactions. They observed that $Cr^{3+}:In_2O_3$ films exhibit ferromagnetism when the films are highly oxygen deficient, and are paramagnetic otherwise. Observation of ferromagnetism in our Mn-doped SnO_2 and Mn-doped In_2O_3 nanocrystalline films imply the important role of interfacial defects for manipulating the long-range magnetic ordering in DMSOs.

Chapter 6
Conclusion and Future Work

6.1 Conclusion

The studies conducted throughout this thesis elaborate on studying structural investigation to determine the occupation sites of Mn dopants and the possible changes in electronic environment around the dopant in Mn-doped SnO_2 and Mn-doped In_2O_3 nanocrystals. Explanation of electronic structure of manganese in diluted magnetic semiconductor oxides (DMSOs) prepared in solution-phase methods can help understand the origin and mechanism of magnetic interactions at room temperature, especially ferromagnetism which theoretically and fundementally has attracted a great interest and effort. According to the literature, manganese ions exist in multiple kinetically oxidation states.

TEM micrographs reveals that synthesized Mn-doped SnO_2 nanocrystals have an average diameter of 2.3±0.6 nm that is smaller than tin oxide Bohr radius (2.7 nm) and XRD pattern clearly shows cassetrite structure. X-ray absorption near edge structure (XANES) analysis confirms co-existance of Mn^{2+} and Mn^{3+} ions substitute the Sn^{4+} site in tin oxide host lattice. Clear difference between spectral shape of Mn-doped SnO_2 NCs and standard manganes oxides excludes the possibility of formation of manganese oxide and manganese clusters during the synthesise process. Increasing the Mn^{2+} nominal concentration from 5 to 15% leads to decrease in $\frac{[Mn^{2+}]}{[Mn^{2+}+Mn^{3+}]}$ fraction from 70 to 50%. The changes in oxidation state are accompanied with the variations in lattice parameters. EXAFS analysis reveals that increase in Mn^{3+} fraction at the expense of Mn^{2+} results in shirinking of the host lattce (the ionic radius of Mn^{3+} is 20% smaller than Mn^{2+}).

Mn-doped In_2O_3 NCs crystallize in two crystal structures. Lower dopant concentration leads to formation of nanocrystals with average diameter of ca. 7.5 nm and XRD patterns reveal cubic bxbyite structure, while increase in dopant concentration up to 20% decreases the nanocrystals size to about 4 nm crystallize in rhombohedral structure. XANES analysis reveals the multiple oxidation states of Mn doped In_2O_3 NCs, independent of the type of Mn percursor. The spectral shape of absorption edge confirms presence of Mn ion in distorted octahedral environment while the presence of manganese oxides and manganese clusters is excluded. Structural parameters have been investigated

by EXAFS spectroscopy. Considering structural parameters of both MnO and Mn_2O_3 gives the best fitting results for fitered Fourier transform.

Presence of Mn^{3+} ions in Mn^{2+}-doped SnO_2 and Mn^{2+}-doped In_2O_3 nanocrystals is further investigated through electronic absorption spectroscopy and magnetic circular dichroism (MCD). While all transitions in Mn^{2+} ($3d^5$) system are spin forbidden, spin-allowed $^5E_g \rightarrow {}^5T_{2g}$ transition observed in UV-Vis absorption spectra and MCD spectra as well, that reveals the presence of Mn^{3+} species. Free standing Mn-doped SnO_2 and Mn-doped In_2O_3 NCs exhibit paramagnetic behavior. A linear combination of two Brillouin functions for Mn^{2+} and Mn^{3+}, $M_s = xM_s(Mn^{2+})+yM_s(Mn^{3+})$, species matches very well with the experimental data and the fractions determined by Brillouin function fitting is inconsistent with XANES results. Fabrication of nanocrystalline films from Mn-doped SnO_2 and Mn-doped In_2O_3 NCs gives rise to formations of interfacial oxygen deficiencies which mediate the long range magnetic ordering of dopant ions and result in ferromagnetic interactions. These defects are also responsible for other functional properties of DMSOs, particularly conductivity, and the ability to control both structure and composition provides new degrees of freedom, and a path for enhancement of the inherent functionalities of complex DMSOs-NCs.

6.2 Future Work

This study can be extended to more oxides and also more dopants. $BaTiO_3$ is one of our candidate and belongs to perovskite family. Different sizes of $BaTiO_3$ nanocrystals are obtained by modifying the solvent composition during the synthesis procedure. Synthesis in water, ethanol and benzyl alcohol dramatically affect the diameter of $BaTiO_3$ NCs and yields nanoparticles with average sizes of 200, 10 and 5 nm, respectively. $BaTiO_3$ NCs were successfully doped using Cr^{3+} ion with different concentrations, and owing to similar ionic radii of Cr^{3+} and Ti^{4+} in octahedral coordination it is well known that the dopant replaces the central Ti^{4+} ions.[75] XRD and TEM characterizations confirm the high purity and crystallinity of the pure and doped $BaTiO_3$.

Changing in size of nanoparticles from 100 to 5 nm leads to a phase transformation from tetragonal to cubic which is confirmed by XRD and Raman spectroscopy. The experimental data suggest that reduction in tetragonality amount is verified by the consistent shifting of the single cubic (200) line and splitting into two tetragonal peaks in XRD patterns and also disappearance of characteristic tetragonal peaks in Raman spectra. The same trace of phase transformtion is observed by increasing dopant concentration.

Ligand-field electronic absorption spectroscopy confirms incorporation of Cr^{3+} in $BaTiO_3$ NCs host lattice through the appearance of $^4A_{2g} \rightarrow {}^4T_{2g}$ transition which is the finger print of Cr^{3+} in octahedral environment. Finally, magnetic saturation collected at 2 K resembles a good match of the experimental data with the spin-only Brillouin function, indicating successful incorporation of Cr^{3+} as isolated paramagnetic ions. Cr^{3+}-doped $BaTiO_3$ can potentially show room temperature ferromagnetism that can be investigated further through fabricating nanocrystalline films. Structural changes during doping process, which are confirmed by XRD and Raman spectroscopy, can be more investigated through XAS spectroscopy.

References

(1) Zhang, J.; Yun, Q.; Wang, Q. **2010**, *4*, 124-130.

(2) Heo, Y. W.; Kelly, J.; Norton, D. P.; Hebard, A. F.; Pearton, S. J.; Zavada, J. M.; Boatner, L. A. *Electrochemical and Solid-State Letters* **2004**, *7*, G309-G312.

(3) Dietl, T.; Ohno, H.; Matsukura, F.; Cibert, J.; Ferrand, D. *Science* **2000**, *287*, 1019-1022.

(4) Pearton, S. J.; Abernathy, C. R.; Overberg, M. E.; Thaler, G. T.; Norton, D. P.; Theodoropoulou, N.; Hebard, A. F.; Park, Y. D.; Ren, F.; Kim, J.; Boatner, L. A. *J. Appl. Phys.* **2003**, *93*, 1-13.

(5) Kiliç, Ç; Zunger, A. *Phys. Rev. Lett.* **2002**, *88*, 955011-955014.

(6) Solymosi, F.; Kiss, J. *Journal of Catalysis* **1978**, *54*, 42-51.

(7) Fuller, M. J.; Warwick, M. E. *Journal of Catalysis* **1973**, *29*, 441-450.

(8) Wyckoff, R. W. G. In *Crystal Structures;* John Wiley & Sons: New York, 1964; .

(9) Suito, K.; Kawai, N.; Masuda, Y. *Mater. Res. Bull.* **1975**, *10*, 677-680.

(10) Floriano, E. A.; De Andrade Scalvi, L. V.; Sambrano, J. R.; Geraldo, V. *Materials Research* **2010**, *13*, 437-443.

(11) Hamberg, I.; Granqvist, C. G. *J. Appl. Phys.* **1986**, *60*, R123-R160.

(12) Weiher, R. L.; Ley, R. P. *J. Appl. Phys.* **1966**, *37*, 299-302.

(13) Murali, A.; Barve, A.; Leppert, V. J.; Risbud, S. H.; Kennedy, I. M.; Lee, H. W. H. *Nano Letters* **2001**, *1*, 287-289.

(14) Li, X.; Wanlass, M. W.; Gessert, T. A.; Emery, K. A.; Coutts, T. J. *Appl. Phys. Lett.* **1989**, *54*, 2674-2676.

(15) Chu, D.; Zeng, Y. -.; Jiang, D.; Xu, J. *Nanotechnology* **2007**, *18*.

(16) Proffit, D. E.; Buchholz, D. B.; Chang, R. P. H.; Bedzyk, M. J.; Mason, T. O.; Ma, Q. *J. Appl. Phys.* **2009**, *106*.

(17) Stanek, C. R.; McClellan, K. J.; Uberuaga, B. P.; Sickafus, K. E.; Levy, M. R.; Grimes, R. W. *Physical Review B - Condensed Matter and Materials Physics* **2007**, *75*.

(18) Shannon, R. D. *Solid State Commun* **1966**, *4*, 629-630.

(19) Epifani, M.; Siciliano, P.; Gurlo, A.; Barsan, N.; Weimar, U. *J. Am. Chem. Soc.* **2004**, *126*, 4078-4079.

(20) Wei, Q.; Brik, M. G.; Guo, L. X.; Wei, B. *Spectrochimica Acta Part A: Molecular and Biomolecular Spectroscopy* **2012**, *97*, 50-53.

(21) Lekshmy, S. S.; Daniel, G. P.; Joy, K. *Appl. Surf. Sci.* **2013**, .

(22) Isono, T.; Fukuda, T.; Nakagawa, K.; Usui, R.; Satoh, R.; Morinaga, E.; Mihara, Y. *Journal of the Society for Information Display* **2007**, *15*, 161-166.

(23) Chen, Z.; Tian, Y.; Li, S.; Zheng, H.; Zhang, W. *J. Alloys Compounds* **2012**, *515*, 57-62.

(24) Farvid, S. S.; Wang, T.; Radovanovic, P. V. In *In Spectroscopic and magnetic properties of colloidal transition metaldoped transparent conducting oxide nanocrystals as building blocks for spintronic materials;* Proceedings of SPIE - The International Society for Optical Engineering; 2010; Vol. 7760.

(25) Pan, H. K.; Knapp, G. S.; Cooper, S. L. *Colloid & Polymer Science* **1984**, *262*, 734-746.

(26) Rockenberger, J.; Zum Felde, U.; Tischer, M.; Tröger, L.; Haase, M.; Weller, H. *J. Chem. Phys.* **2000**, *112*, 4296-4304.

(27) Davis, S. R.; Chadwick, A. V.; Wright, J. D. *J Phys Chem B* **1997**, *101*, 9901-9908.

(28) Parent, P.; Dexpert, H.; Tourillon, G.; Grimal, J. -. *J. Electrochem. Soc.* **1992**, *139*, 276-281.

(29) Farvid, S. S.; Radovanovic, P. V. *J. Am. Chem. Soc.* **2012**, *134*, 7015-7024.

(30) Fukumura, T.; Jin, Z.; Ohtomo, A.; Koinuma, H.; Kawasaki, M. *Appl. Phys. Lett.* **1999**, *75*, 3366-3368.

(31) Matsumoto, Y.; Murakami, M.; Shono, T.; Hasegawa, T.; Fukumura, T.; Kawasaki, M.; Ahmet, P.; Chikyow, T.; Koshihara, S. -.; Koinuma, H. *Science* **2001**, *291*, 854-856.

(32) Ogale, S. B.; Choudhary, R. J.; Buban, J. P.; Lofland, S. E.; Shinde, S. R.; Kale, S. N.; Kulkarni, V. N.; Higgins, J.; Lanci, C.; Simpson, J. R.; Browning, N. D.; Das Sarma, S.; Drew, H. D.; Greene, R. L.; Venkatesan, T. *Phys. Rev. Lett.* **2003**, *91*, 772051-772054.

(33) Archer, P. I.; Radovanovic, P. V.; Heald, S. M.; Gamelin, D. R. *J. Am. Chem. Soc.* **2005**, *127*, 14479-14487.

(34) Coey, J. M. D.; Venkatesan, M.; Fitzgerald, C. B. *Nature Materials* **2005**, *4*, 173-179.

(35) Dave, N.; Pautler, B. G.; Farvid, S. S.; Radovanovic, P. V. *Nanotechnology* **2010**, *21*.

(36) Archer, P. I.; Radovanovic, P. V.; Heald, S. M.; Gamelin, D. R. *J. Am. Chem. Soc.* **2005**, *127*, 14479-14487.

(37) Seo, W. S.; Jo, H. H.; Lee, K.; Park, J. T. *Adv Mater* **2003**, *15*, 795-797.

(38) Farvid, S. S.; Ju, L.; Worden, M.; Radovanovic, P. V. *Journal of Physical Chemistry C* **2008**, *112*, 17755-17759.

(39) Farvid, S. S.; Dave, N.; Radovanovic, P. V. *Chemistry of Materials* **2010**, *22*, 9-11.

(40) Farvid, S. S.; Hegde, M.; Radovanovic, P. V. *Chemistry of Materials* **2013**, *25*, 233-244.

(41) G. Bunker In *Iintroduction to XAFS:
A Practical Guide to X-ray Absorption Fine Structure Spectroscopy;* Cambridge University Press: 2010; .

(42) Behrens, P. *Trends in Analytical Chemistry* **1992**, *11*, 237-244.

(43) D. N. Sathyanarayana In ***Electronic Absorption Spectroscopy and Related Techniques****;* Universities Press (India) Limited: India, 2001; .

(44) McMaster, J.; Oganesyan, V. S. *Curr. Opin. Struct. Biol.* **2010**, *20*, 615-622.

(45) Sabergharesou, T.; Wang, T.; Ju, L.; Radovanovic, P. V. *Appl. Phys. Lett.* **2013**, *103*.

(46) Dey, T.; Khuntia, P.; Mahajan, A. V.; Kumar, N.; Sundaresan, A. *EPL* **2011**, *96*.

(47) B.D. Cullity, S. R. S., Ed.; In *Elements of X-Ray Diffraction;* Prentice-Hall Inc.: 2001; .

(48) R. Jenkins, R. L. S. In *Introduction to X-ray Powder Diffractometry;* John Wiley & Sons Inc.: 1996; .

(49) Wong, J.; Lytle, F. W.; Messmer, R. P.; Maylotte, D. H. *Physical Review B* **1984**, *30*, 5596-5610.

(50) Pantelouris, A.; Küper, G.; Hormes, J.; Feldmann, C.; Jansen, M. *J. Am. Chem. Soc.* **1995**, *117*, 11749-11753.

(51) C. Mande, V. B. Sapre In *Advances in X-ray Spectroscopy;* C. Bonnelle, C. M., Ed.; Pergamon: New york, 1983; pp 287-301.

(52) Whittaker, L.; Wu, T. -.; Patridge, C. J.; Sambandamurthy, G.; Banerjee, S. *Journal of Materials Chemistry* **2011**, *21*, 5580-5592.

(53) Campos, A.; Lohitharn, N.; Roy, A.; Lotero, E.; Goodwin Jr., J. G.; Spivey, J. J. *Applied Catalysis A: General* **2010**, *375*, 12-16.

(54) Gilbert, B.; Frazer, B. H.; Belz, A.; Conrad, P. G.; Nealson, K. H.; Haskel, D.; Lang, J. C.; Srajer, G.; De Stasio, G. *Journal of Physical Chemistry A* **2003**, *107*, 2839-2847.

(55) Sherman, D. M. *Am. Mineral.* **1984**, *69*, 788-799.

(56) Baron, V. *Am. Mineral.* **1998**, *83*, 786-793.

(57) Dau, H.; Liebisch, P.; Haumann, M. *Analytical and Bioanalytical Chemistry* **2003**, *376*, 562-583.

(58) Farvid, S. S.; Dave, N.; Wang, T.; Radovanovic, P. V. *Journal of Physical Chemistry C* **2009**, *113*, 15928-15933.

(59) An, Y.; Feng, D.; Duan, L.; Wu, Z.; Liu, J. *J. Phys. D* **2012**, *45*.

(60) Nadaud, N.; Lequeux, N.; Nanot, M.; Jové, J.; Roisnel, T. *Journal of Solid State Chemistry* **1998**, *135*, 140-148.

(61) Prewitt, C. T.; Shannon, R. D.; Rogers, D. B.; Sleight, A. W. *Inorg. Chem.* **1969**, *8*, 1985-1993.

(62) Vaida, M. *Optoelectronics and Advanced Materials, Rapid Communications* **2012**, *6*, 713-716.

(63) Yen, W. M.; Shionoya, S.; Yamamoto, H., Eds.; In ***Phosphor Handbook*** *;* Taylor & Francis Group: 2007; .

(64) Lever, A. B. P. In *Inorganic Electronic Spectroscopy;* Elsevier: Amsterdam, 1984; .

(65) Reddy, S. L.; Endo, T.; Reddy, G. S. In ***Advanced Aspects of Spectroscopy****;* Muhammad Akhyar Farrukh, Ed.; InTech: 2012; .

(66) Piper, T. S.; Carlin, R. L. *J. Chem. Phys.* **1961**, *35*, 1809-1815.

(67) McClure, D. S. *J. Chem. Phys.* **1962**, *36*, 2757-2779.

(68) Las, W. C.; Gouvea, D.; Sano, W. *Solid State Sciences* **1999**, *1*, 331-337.

(69) Eichel, R. -. *Physical Chemistry Chemical Physics* **2011**, *13*, 368-384.

(70) Radovanovic, P. V.; Gamelin, D. R. *Phys. Rev. Lett.* **2003**, *91*, 1572021-1572024.

(71) Ju, L.; Sabergharesou, T.; Stamplecoskie, K. G.; Hegde, M.; Wang, T.; Combe, N. A.; Wu, H.; Radovanovic, P. V. *J. Am. Chem. Soc.* **2012**, *134*, 1136-1146.

(72) Abraham, D. W.; Frank, M. M.; Guha, S. *Appl. Phys. Lett.* **2005**, *87*, 1-3.

(73) Kobayashi, M.; Ishida, Y.; Hwang, J. I.; Song, G. S.; Takizawa, M.; Fujimori, A.; Takeda, Y.; Ohkochi, T.; Okane, T.; Saitoh, Y.; Yamagami, H.; Gupta, A.; Cao, H. T.; Rao, K. V. *Physical Review B - Condensed Matter and Materials Physics* **2009**, *79*.

(74) Philip, J.; Punnoose, A.; Kim, B. I.; Reddy, K. M.; Layne, S.; Holmes, J. O.; Satpati, B.; Leclair, P. R.; Santos, T. S.; Moodera, J. S. *Nature Materials* **2006**, *5*, 298-304.

(75) Buscaglia, M. T.; Buscaglia, V.; Viviani, M.; Nanni, P. *J Am Ceram Soc* **2001**, *84*, 376-384.